

## Salt Polygons and Porous Media Convection

Jana Lasser<sup>1,2,\*</sup> Joanna M. Nield<sup>3</sup> Marcel Ernst<sup>2</sup> Volker Karius<sup>4</sup> Giles F. S. Wiggs<sup>5</sup>  
 Matthew R. Threadgold<sup>6</sup> Cédric Beaume<sup>6</sup> and Lucas Goehring<sup>7,†</sup>

<sup>1</sup>Graz University of Technology, Institute for Interactive Systems and Data Science,  
 Inffeldgasse 16c, 8010 Graz, Austria

<sup>2</sup>Max Planck Institute for Dynamics and Self-Organization Am Fassberg 17, 37077 Göttingen, Germany

<sup>3</sup>Geography and Environmental Science, University of Southampton Highfield,  
 Southampton SO17 1BJ, United Kingdom

<sup>4</sup>Geowissenschaftliches Zentrum, Georg-August-University,  
 Goldschmidtstrasse 3, 37077 Göttingen, Germany

<sup>5</sup>School of Geography and the Environment, University of Oxford,  
 South Parks Road, Oxford OX1 3QY, United Kingdom

<sup>6</sup>School of Mathematics, University of Leeds, Leeds LS2 9JT, United Kingdom

<sup>7</sup>School of Science and Technology, Nottingham Trent University,  
 Nottingham NG11 8NS, United Kingdom

 (Received 1 June 2022; revised 5 December 2022; accepted 25 January 2023; published 24 February 2023)

From fairy circles to patterned ground and columnar joints, natural patterns spontaneously appear in many complex geophysical settings. Here, we investigate the origins of polygonally patterned crusts of salt playa and salt pans. These beautifully regular features, approximately a meter in diameter, are found worldwide and are fundamentally important to the transport of salt and dust in arid regions. We show that they are consistent with the surface expression of buoyancy-driven convection in the porous soil beneath a salt crust. By combining quantitative results from direct field observations, analog experiments, and numerical simulations, we further determine the conditions under which salt polygons should form, as well as how their characteristic size emerges.

DOI: [10.1103/PhysRevX.13.011025](https://doi.org/10.1103/PhysRevX.13.011025)

Subject Areas: Fluid Dynamics, Geophysics,  
 Nonlinear Dynamics

## I. INTRODUCTION

Salt deserts or dry salt lakes are among the most inhospitable places on our planet. Their otherworldly shapes inspire the imagination (e.g., *Star Wars*' desert planet Crait, or the million tourists annually visiting Death Valley [1]) and are an important driver of climate processes [2–8]. Various referred to as salt pans, playas, or dry lakes, the immediately prominent feature of such landscapes (Fig. 1) is a characteristic tiling of polygons formed by ridges in the salt-encrusted surface. These patterns are seen around the world [9–16], including Salar de Uyuni in Chile [9], Chott el Djerid in Tunisia [10], Badwater Basin in California [11], Dasht-e Kavir in Iran [12], and

Dalangtan Playa in China [13]. Although they have been argued to share similarities with fracture [12] or buckling [17] patterns, a quantitative and predictive mechanism for the emergence of the patterns remains obscure.

A challenge to any explanation is that the polygonal patterns in salt crusts are remarkably similar wherever they occur, despite local differences in geology, salt chemistry, and environmental conditions. For example, while crusts can vary from subcentimeter to meters in thickness [2,12,18], they predominantly express polygons about 1–2 m across [2,11,12,15–20]. The same patterns also appear for pure halite crusts such as those of Badwater Basin [11] and pans in Iran [12] as well as the sulfate-rich crusts found, for example, at Owens Lake (California) [11], Sua Pan (Botswana) [21], the coastal sabkhas of Abu Dhabi [14] and Salar de Uyuni [9].

The salt crusts of dry lakes are known to be dynamic over months to years [2,15,17,18,22,23] and couple to other environmental processes. They form in areas with a negative water balance (i.e., where evaporation significantly exceeds precipitation), and the dominant water balance is between a perennial groundwater flow seeping in from distant sources and the evaporation of this water

\*jana.lasser@tugraz.at

†lucas.goehring@ntu.ac.uk

Published by the American Physical Society under the terms of the *Creative Commons Attribution 4.0 International* license. Further distribution of this work must maintain attribution to the author(s) and the published article's title, journal citation, and DOI. Open access publication funded by the Max Planck Society.



FIG. 1. Typical salt polygon patterns at (a) Middle Basin in Death Valley, (b) Owens Lake, and (c) Badwater Basin in Death Valley, California [Image (a) courtesy Sarah Marino].

from the surface of the dry lake [2,4,24]. The groundwater brings dissolved salts with it, which accumulate at the surface in a crust of evaporites. Wind blowing over the crust entrains dust, which forms a significant proportion of the global atmospheric dust production [3,6,7] and of mineral transport to the oceans [25]. As one example, dust from the dry Owens Lake has posed health problems for people living nearby [26,27], and the site is the center of a decades-long, intense remediation effort [28]; a preferred method is the use of shallow flooding to encourage formation of a continuous, active surface crust [29,30].

While playas are inherently associated with dust sources, these sources are temporally and spatially variable [24,31–33], and there is a lack of understanding of the relevant processes of how crusts form, are sustained, and degrade [7,34]. The height of polygon ridges affects the threshold wind speed for dust entrainment [7,35], and complete coverage of a crust reduces the sediment available for dust emission compared to a patchy crust. In order to better account for these complexities, we need to understand the relationships between surface and subsurface drivers of playa dust sources [7,31].

Salt crusts also modify evaporation and heat flux from the playa surface [5], and hence, the water and energy balances of these fragile environments. In particular, experimental and field research consistently show that continuous crusts reduce evaporation rates on playa surfaces by an order of magnitude compared to climate-derived estimates [8,29,35–37]. As a result, the observed groundwater evaporation rates at sites with active and continuous salt crusts tend to lie in the relatively low range of 0.2–0.7 mm/day, including seasonal variations [29,37–41].

Research on salt pans has typically focused on either the dynamics of their complex subsurface flows [42–46] or their crusts [15,17,18,35], without considering how these features interact. Here we show that by treating the surface

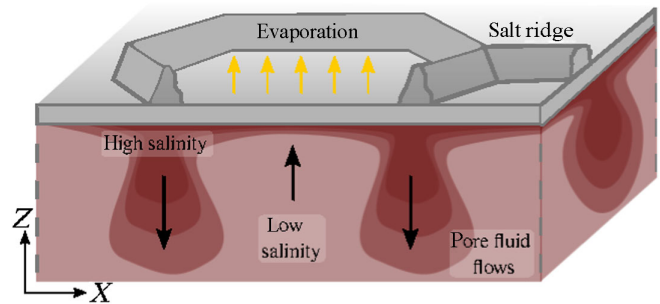


FIG. 2. Proposed dynamics of patterned salt crusts. The dominant fluid motions are shown by the black arrows, and the water salinity is indicated by the color contours.

of a salt playa together with the fluid in the porous medium of the soil near its surface, the origins, dynamics, length scale, and shape of the polygonal patterns in salt crusts can be apprehended. As we develop and test such a model of salt crust formation, we show how it makes explicit predictions of crust growth rates, the conditions necessary to form ridges and continuous crusts, and other inputs into dust or groundwater models of these extreme environments. In particular, by combining theoretical analysis, numerical simulations, experiments, and field observations, we demonstrate how the density-driven convective dynamics of groundwater can lead to variations in the salt flux into the crust, with faster precipitation along the boundaries between convective cells facilitating the growth of a polygonal network of salt ridges (see Fig. 2). Under measured field conditions, the size of the expected convective cells matches the scale observed for the surface crust patterns and makes accurate predictions about the crust growth rates. Finally, we present direct field-based evidence of convective dynamics that are correlated to the surface crust patterns.

## II. PHENOMENOLOGY OF SALT POLYGONS

Any model for the emergence of salt crust patterns should be able to convincingly explain their commonly observed features. Polygonal networks are one of the more common emergent patterns in geophysics, seen for columnar jointing [47], ice-wedge polygons [48,49], polygonal terrain [50], some types of mud cracks [51], as well as convection [52,53], for example. As such, a suite of more detailed or quantitative predictions are important to evaluate any model that displays polygonal features.

Based on the known phenomenology of salt playa, the most significant tests for a predictive model include (i) the driving mechanism should be specific to the geophysical conditions encountered in salt lakes [9–12,14–16] and (ii) should spatially modulate salt transport, leading to increased salt precipitation at ridges in the crust [2,12,54]. (iii) The response should be fast enough and stable enough to account for ridge growth on a scale of months [2,15,18,22].

(iv) The model dynamics should generate closed polygonal patterns of relatively narrow ridges spaced a few meters apart [11,12,15–18], and (v) the characteristics and scale of the patterns should be robust to environmental variations, including different types of soil ranging from silt to sand [11], salt compositions ranging from pure halite crusts to those with significant amounts of sulfates (e.g. trona) and carbonates (e.g., trona) [9,11,12,14,37], and any local differences in climate and variables like the evaporation rate [29,37–39].

Previous models of salt polygons have mainly considered mechanical effects. The earliest argument was made by Christiansen in 1963 [17]. He suggested that the shapes were the result of compressive stress due to salt precipitation and temperature changes, which caused the crust to first buckle and then crack as the growing ridges thrust upward. He noted that the spacing of the buckling features should be proportional to the thickness of the stressed crust and also depend on its strength; these predictions are consistent with the modern understanding of wrinkling phenomena [55–57]. However, wrinkles due to isotropic compression typically form parallel features, such as stripes, rather than closed shapes [55–57]; polygons can form by compression, but only by folds into an elastic layer, rather than ridges projecting out of a layer [57,58]. A more fracture-focused model was proposed by Krinsley [12] in his 1970 survey of Iranian salt pans. He argued that desiccation places the crust into tension, rather than compression, which is relieved by fracture. The cracks then allow for groundwater to more easily reach the surface to evaporate, so that ridges grow up around them. As the crust develops faster at the ridges, these can buckle or thrust upward [as in Fig. 1(b)]. Like wrinkling, for cracks the expected feature size is a few times the thickness of the cracking layer [59,60].

Both the wrinkling [2,54] and fracture [18–20,61] models can explain the qualitative appearance of cracks and thrusting at the ridges in salt crusts. The main difficulty with any purely mechanical model, however, is length-scale selection. The natural spacing between buckles or cracks is proportional to the thickness of the layer under stress [55–60]. As some geophysical examples, the scale of ice-wedge polygons in permafrost is determined by the depth at which annual temperature changes diffuse into the ground [48,62], whereas the size of columnar joints in lava records how it cooled, and in particular, the thickness of a cooling front invading into an initially molten lava formation [47]. For salt playa, crust thicknesses vary widely, so they cannot explain the robust polygonal scale seen in nature, and no other convincing explanation for the feature spacing has been proposed.

As an important mechanism, one may also consider the crust composition itself, which can include minerals in different hydration states. For example, thenardite ( $\text{Na}_2\text{SO}_4$ ) transforms into mirabilite ( $\text{Na}_2\text{SO}_4 \cdot 10\text{H}_2\text{O}$ ),

and expands its volume by approximately 320%, at temperatures easily seen in salt deserts [63]. While phase changes can undoubtedly generate stresses, the difficulty of length-scale selection remains, given similar patterns in crusts of different thickness. In addition, salt polygons are routinely seen in crusts with almost pure halite (NaCl) composition [11,12], where such effects are absent.

### III. BUOYANCY-DRIVEN CONVECTION AS A MECHANISM FOR PATTERN FORMATION

As discussed, explanations for the formation of salt polygons have so far focused on mechanical effects. Crust growth is implied in these cases, but the salt source feeding this growth is not modeled explicitly. In other contexts, there is well-developed literature regarding buoyancy-driven convection in porous media, including salt lakes [44,45,64], sabkhas [46,65], carbon sequestration applications [52,66,67], and thermally driven cases [42,53,68]; the model we develop here builds on a recent study of the linear stability and approach to a statistically steady state of convection in a dry salt lake [64]. However, the effects of such flows on a salt crust have not yet been explored. Here, we examine the implications of convection in the soil beneath a salt crust and its predictions for the emergence of salt polygons.

We consider a coupling of surface salt patterns to subsurface flows, as visualized in Fig. 2. Briefly, surface evaporation will leave the near-surface groundwater enriched in salt, and heavier than the fluid beneath it. This can lead to precipitation of salt at the surface as well as convection in the soil, with narrow, regularly spaced downwellings of high salinity [64]. We show that convection should result in a higher salt flux into the surface above the downwellings, where salinity gradients in the groundwater are weaker. We argue that this preferential precipitation of salt templates the growth of ridges at the locations of the downwellings. At upwelling plumes, the larger salinity gradients strengthen the diffusive transport away from the surface, rather than advective transport toward it, and crust growth is slower.

Our main field site, Owens Lake [Fig. 1(b)], has a typical crust pattern in a well-studied and controlled landscape, and can introduce our modeling assumptions. This dry, terminal saline lake has an aquifer extending from the near surface to over 150 m depth [69]. The groundwater carries dissolved salts [27,37,70], which collect in an evaporite pan of about 300 km<sup>2</sup> [3,69] and which are particularly concentrated in the fluid within a meter or so of the surface [11,37]. Average annual groundwater evaporation rates of  $E = 0.4 \pm 0.1$  mm/day have been measured in areas with active salt crusts [37]. The near-surface soil is a silt to fine sand with high porosity of  $\phi = 0.7$  [37]. A tortuosity-corrected diffusion constant  $D = 1.00 \pm 0.24 \times 10^{-9}$  m<sup>2</sup>s<sup>-1</sup> is representative of the mix of dissolved salts present at the site (mainly NaCl and Na<sub>2</sub>SO<sub>4</sub>). Efforts to control dust

emission from the lake involve shallow flooding [30], vegetation [71], gravel cover, and encouraging crust growth [29]. As shown in Supplemental Material Video S1 [72], after a shallow-flooding event the soil is saturated with water, which evaporates and leaves behind salts that crystallize into a continuous crust covered by a network of slowly growing ridges. Given the high quality of the observational record at Owens Lake, and in order to make quantitative predictions relevant to the remediation of this important site, we use representative values from it throughout this section.

### A. Governing equations

The transport of fluid beneath a dry salt lake can be treated as a Darcy flow in a porous medium, with evaporation occurring at the surface and being fed from below by water with some background salinity (see, e.g., Refs. [42,44,64,73]). Such a system will naturally develop a salinity gradient below the surface, which can become unstable to convective overturning [42,44,64].

As a prototype case, we consider a large, flat salt lake with an average surface evaporation rate  $E$ , and where the groundwater is recharged from some deep, distant reservoir. For the subsurface flows, we model the volumetric flux, or superficial fluid velocity  $\mathbf{q}$ , of a fluid of pressure  $p$  moving through a porous medium of constant uniform porosity  $\varphi$  and permeability  $\kappa$ . By mass conservation,  $E$  is also the average of the upward component of the fluid flux  $q_z$  at any depth as well as the recharge rate from the reservoir. The fluid has a viscosity  $\mu$  and carries dissolved salt, whose diffusivity  $D$  can be corrected for the presence of different ions as well as tortuosity [74,75].

The dissolved salt contributes to the density of the fluid  $\rho$  and hence to buoyancy forces. In salt lakes, thermal buoyancy is several orders of magnitude weaker than solutal buoyancy and can be neglected [44,64]. Using the Boussinesq approximation,  $\rho = \rho_0 + S\Delta\rho$ , where  $\rho_0$  is the density of the reservoir fluid (including its dissolved salts; see Sec. III C), and  $\rho_1 = \rho_0 + \Delta\rho$  is the density of a saturated solution. The relative salinity  $S$  mediates between these limits:  $S = 0$  corresponds to the background salinity of fluid entering from a distant source ( $z \rightarrow -\infty$ ), whereas  $S = 1$  represents a salt-saturated brine in contact with the crust (at  $z = 0$ ).

The governing equations are then a continuity equation for incompressible fluid flow, an advection-diffusion equation for the relative salinity, and Darcy's law:

$$\nabla \cdot \mathbf{q} = 0, \quad (1)$$

$$\varphi \frac{\partial S}{\partial t} = \varphi D \nabla^2 S - \mathbf{q} \cdot \nabla S, \quad (2)$$

$$\mathbf{q} = -\frac{\kappa}{\mu} (\nabla p + \rho g \hat{\mathbf{z}}), \quad (3)$$

where  $g$  is the acceleration due to gravity, and  $\hat{\mathbf{z}}$  is an upward-pointing unit vector. These mass and momentum balances can describe a variety of porous media flows, including solutal flows in playas and sabkhas [44,45,64,73,76], CO<sub>2</sub>-rich flows in carbon sequestration applications [67,77], and, with an appropriate transformation of variables, flows driven by thermal buoyancy [42,68,78]. A review of these phenomena was recently given in Ref. [79]. As boundary conditions for the salt lake scenario, we take

$$\begin{aligned} S &= 1, & q_z &= E \text{ on } z = 0, \\ S &\rightarrow 0, & q_z &\rightarrow E \text{ as } z \rightarrow -\infty. \end{aligned}$$

In order to nondimensionalize the governing equations, one needs to specify a characteristic length scale  $L$  and velocity scale  $\mathcal{V}$ , with a natural timescale following as  $T = \varphi L / \mathcal{V}$ . Taking advantage of how the evaporation rate sets the average vertical fluid flux everywhere, we use  $\mathcal{V} = E$ . Then, in the absence of any geometric length scale in the problem (e.g., the layer thickness often used for two-sided convection [79]), we set  $L = \varphi D / E$  as the distance over which advective and diffusive effects will balance for fluids moving at the characteristic speed  $E$ . Rescaling Eqs. (1)–(3) then leads to

$$\nabla \cdot \mathbf{U} = 0, \quad (4)$$

$$\frac{\partial S}{\partial \tau} = \nabla^2 S - \mathbf{U} \cdot \nabla S, \quad (5)$$

$$\mathbf{U} = -\nabla P - \text{Ra} S \hat{\mathbf{z}}, \quad (6)$$

with a rescaled velocity  $\mathbf{U} = \mathbf{q} / E$ , depth  $Z = zE / \varphi D$ , time  $\tau = tE^2 / \varphi^2 D$ , and pressure  $P = (\kappa / \varphi \mu D)(p + \rho_0 g z)$ . This system of equations is governed by a single dimensionless group, the Rayleigh number:

$$\text{Ra} = \frac{\kappa \Delta \rho g}{\mu E}. \quad (7)$$

Here, the Rayleigh number also gives the ratio of the speed at which a large heavy plume will fall under its own weight  $\mathcal{V}_B = \kappa \Delta \rho g / \mu$  to the upward drift due to surface evaporation:  $\text{Ra} = \mathcal{V}_B / E$ . Thus, it is frequently used to characterize the vigor of porous medium convection with a throughflow [42–44,64,73].

A more detailed derivation of this model, along with discussion of the assumptions behind it, a linear stability analysis of the onset of convection, and a two-dimensional numerical investigation into its statistically steady state, was recently published by some of us [64]. Our aim here is to show how solutal convection beneath a salt lake will couple to the growth of patterns in the crust and to make predictions which can be compared to field measurements.

As such, after a discussion of how the emergent dynamics of this model will appear in geophysically relevant conditions, we develop predictions of the salt flux into the crust, which can give rise to crust patterns.

### B. Convective dynamics and scale selection

The model above is designed to match the expected dynamics of groundwater in a dry salt lake with at least a thin salt crust developing on top of a fluid-saturated soil. For the one-dimensional case, where salinity depends only on depth, there is a unique stationary solution to Eqs. (4)–(6), namely,  $S = e^Z = \exp(zE/\varphi D)$ ,  $\mathbf{U} = (0, 0, 1)$ , and  $P = \text{Ra}(1 - e^Z) - Z$ , which represents a salt-rich layer of groundwater lying just below the surface and a balance between advective and diffusive transport of salt [42]. In the absence of any horizontal flows, other plausible initial conditions, such as an initially uniform lake (i.e.,  $S = 0$  everywhere), will relax toward the stationary solution on the characteristic timescale  $T$  [44,64]. Similarly, an initially crust-free lake can be described at first by an unsaturated boundary at  $Z = 0$ , with no flux into the surface until the salinity there reaches saturation: This scenario will also develop a boundary layer that reaches saturation, and starts to precipitate over the same timescale [44]. For representative parameter values from Owens Lake,  $T$  is about six months, consistent with the known timescale of crust development [15], and  $L = 15 \pm 8$  cm.

For a wide variety of initial conditions, therefore, a dry salt lake will naturally develop a heavy salt-rich boundary layer of fluid near its surface. Above some critical Rayleigh number  $\text{Ra}_c$  this layer will be unstable to convection [42–44,64,73]. Linear stability analysis shows that for constant, uniform evaporation at the surface, the stationary solution has a finite-wavelength instability above  $\text{Ra}_c \simeq 14.35$  that leads to the growth of convective plumes [42,43,64]. At  $\text{Ra}_c$  the critical wave number  $a_c \simeq 0.76$  for conditions at Owens Lake, corresponding to a wavelength of 1.3 m. Intriguingly, this characteristic scale of the convective instability is of the same order of magnitude as the patterns typically seen in salt crusts.

This instability is also robust to different assumptions about the initial and boundary conditions of the lake. For example, an initially uniform lake (where  $S = 0$  at  $t = 0$ ) has the same  $\text{Ra}_c$  as the stationary state, along with a very similar spectrum of unstable modes [64]. Alternatively, as would be appropriate for a salt lake with a thin ponding of surface brine, the case of a constant pressure boundary condition at  $Z = 0$  is unstable to convection above  $\text{Ra}_c \simeq 6.95$ , with  $a_c \simeq 0.43$  [42].

To predict the long-time dynamics of convection pattern in a dry salt lake, we simulate Eqs. (4)–(6) on rectangular domains (2D) or boxes (3D), where  $S = U_Z = 1$  at the top boundary,  $S = 0$  and  $U_Z = 1$  at the bottom, and with periodic boundary conditions along the vertical walls. We conduct simulations from  $\text{Ra} = 20$  to 1000. As initial

conditions, we start from the stationary state for a bounded domain  $S = (e^Z - e^{-h})/(1 - e^{-h})$ , with small random perturbations applied to the salinity distribution at all grid points. Most simulation domains have a horizontal extent of  $12\pi$  (for 2D) or  $24\pi$  (for 3D) and depth of  $h = 10$ . The domain depth introduces an additional length scale, and dimensionless group, into the numerical problem. To confirm that the results are in a limit where they are essentially independent of  $h$ , we repeat selected simulations for domains with  $h = 20$ . Our numerical methods are summarized in Appendix A.

A finite-wavelength instability sets in for all simulations and rapidly grows beyond the linear regime. As shown for the 2D case in Figs. 3(a)–3(c), perturbations around the most unstable mode develop into a set of narrow plumes of high salinity, which fall from the upper surface. In 3D the situation is similar, as in Figs. 3(d) and 3(e), with the convection near the surface instead organizing into a closed polygonal network of downwelling sheets, which surround patches of upwelling fluid. At lower depths the sheets break up into isolated plumes. Both the growth rate of the linear instability and the speed of the mature downwelling features scale with  $\epsilon = (\text{Ra} - \text{Ra}_c)/\text{Ra}_c$ , which can be understood as  $\text{Ra} \sim \mathcal{V}_B$ . As such, we make use of a rescaled time  $\hat{\tau} = \tau\epsilon$  in order to compare features at a similar stage of development.

As they grow, the initial downwelling features strip the boundary layer of dissolved salt, leaving it depleted of the buoyancy forces that initiated the convection. The plumes also tend to merge together into larger structures. This coarsening process causes the pattern length scale to increase over time; for further details, see Ref. [64]. However, as the distance between downwelling areas grows, they become less efficient at draining salinity from the boundary layer, which can start to thicken again. This allows for the growth of additional instabilities. In 2D these take the form of small plumes that appear between, and are attracted to, the larger established downwellings. In 3D, although new pointlike plumes do also occur, the initiation of linear features is more typical. As shown in Figs. 3(d) and 3(e), these structures appear as weaker downwelling sheets that connect two sides of polygonal convection cells. As they grow, they also move toward the boundaries of the more established, larger convection cells, eventually merging with an existing edge. These transient “microplume” features become more prevalent at higher  $\text{Ra}$ , overlaid on the more stable “megaplumes” of convection cells [53], which extend much deeper than the boundary layer. Over long enough times, a statistically steady state develops [64] where the rates of plume formation and merging balance, and a well-defined length scale emerges.

These dynamics can be compared with analogous results from two-sided convection without throughflow [52,53,68,80], which has become an important model of carbon geosequestration. For this, some caution is required,

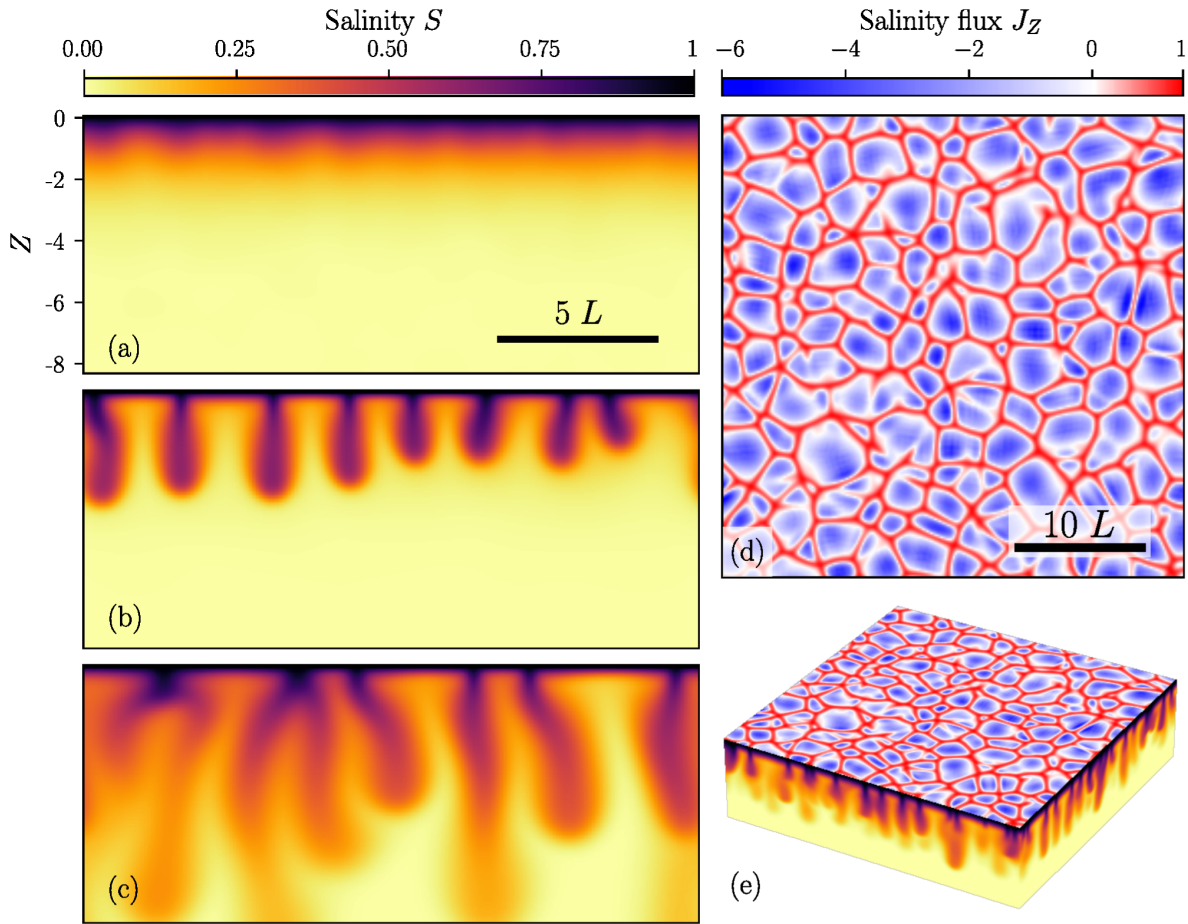


FIG. 3. The dynamics of porous media convection simulated below a salt lake are shown for  $Ra = 100$ . For two-dimensional simulations, the development of high-salinity ( $S$ ) downwelling plumes is shown for times (a)  $\tau = 0.1$ , (b)  $\tau = 0.3$ , and (c)  $\tau = 1.0$ . Supplemental Material Video S2 [72] shows the full dynamics of the simulation. Panel (d) shows a snapshot of three-dimensional salinity flux into the surface ( $Z = 0$ ) for  $\tau = 1.0$ . Panel (e) shows the same snapshot, now including a view of the downwellings of high salinity along the vertical faces of the domain. Here, the downwellings arrange into narrow sheets, forming a network around more diffuse upwelling regions. Supplemental Material Video S3 [72] shows the full dynamics of the three-dimensional simulation.

as the characteristic scales and Rayleigh number are defined differently in the two cases. Comparing the two systems, the patterns near the walls are remarkably similar, with transient ribs or sheets appearing between larger, more stable and regular polygonal cells [52,53,68]. Interestingly, however, the wavelength selection process is quite different. For two-sided convection the dominant circulation cells sampled at the midplane scale with a wavenumber  $a \sim Ra^{0.5}$ . Near the walls, the density of the smaller, transient features increases more rapidly with  $Ra$ , with a dependence thought to approach  $a \sim Ra$  at high enough  $Ra$  [52,53,79]. However, averaging out these fast-moving features over time, or through spatial filtering, shows a near-surface pattern that closely matches the internal convection cells [53].

For our one-sided salt lake model, quantitative details of the scale selection process are presented in Fig. 4, which also includes the neutral stability curve and most unstable mode of convection, as derived in Ref. [64]. Simulations with  $Ra > Ra_c$  are unstable to convective overturning, which

becomes more vigorous with increasing  $Ra$ . To begin with, average pattern wave numbers  $\langle a \rangle$  were calculated as in Ref. [68], as the first moments of the radially averaged power spectra of the salinity distributions at a depth of  $Z \approx 1$  (see Appendix A). The initial instability is characterized at the rescaled time  $\hat{\tau} = 1$ . At these early times, the spacing of downwellings in both the 2D and 3D simulations (red markers) agrees well with the most unstable mode of the linear stability analysis. When measured at  $\hat{\tau} = 30$ , however, many downwelling plumes have merged, leading to smaller wave numbers (blue markers). Confirming that the system is in a statistically steady state by this time, simulations run to  $\hat{\tau} = 60$  show no measurable systematic drift in  $\langle a \rangle$  (values match with  $\hat{\tau} = 30$  to  $\Delta k = -0.004 \pm 0.01$ , mean  $\pm$  standard error). Similarly, additional simulations with  $h = 20$  give comparable results (values match with  $h = 10$  to  $\Delta k = -0.04 \pm 0.04$ ).

In the steady state, there is a gradual increase in the average wave number with  $Ra$ , as is the case also for

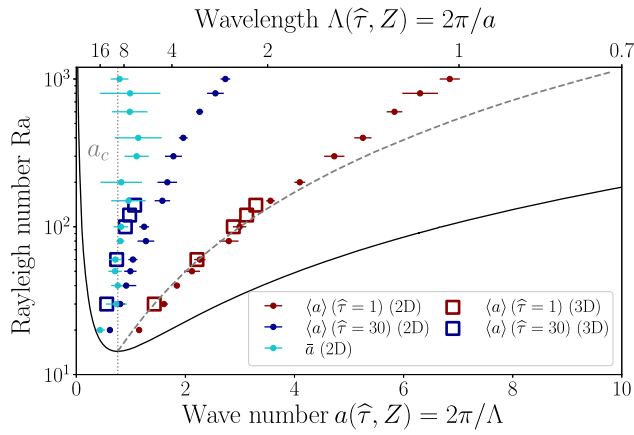


FIG. 4. Pattern wave numbers  $a$  as measured in two-dimensional (circles) and three-dimensional (squares) simulations for different  $Ra$ . Average wave numbers  $\langle a \rangle$  are measured at two times: once early into the growth of the initial instability at  $\hat{\tau} = 1$  (red), and later at  $\hat{\tau} = 30$  (blue) after the pattern has time to develop toward a statistically steady state. We also report the wave number of the dominant mode  $\bar{a}$  (turquoise) at late times. For the 2D simulations, the marker positions and error bars represent means and standard deviations as measured in ensembles of six to ten realizations each.

two-sided convection, although this trend is systematically weaker than the scalings evident there [52,53,68]. This increase appears to be driven by the proliferation of small, transient downwelling microplumes as  $Ra$  increases. These intermittently appear, then are swept into the more established large-scale convective features (see Supplemental Material Videos S2 and S3 [72]). As the surface crust is built up over time, we expect it to reflect the more stable features, i.e., megaplumes. To isolate the size of these features, we calculate the dominant wave number  $\bar{a}$  associated with the maximum of the power spectrum (i.e., the mode). As shown in Fig. 4 (turquoise markers), this predicts a pattern of polygonal cells bounded by salt-rich downwellings, and a characteristic wavelength that

consistently settles to values near  $\Lambda = 2\pi/a_c$ , or about 1.3 m for the conditions typical of Owens Lake.

### C. Salt flux and ridge growth

At the surface of the soil, water will evaporate and leave behind its dissolved burden of salt. In our model of this process, the rate at which salt is added to the surface depends on its advection along with the water, but it is also influenced by diffusion down concentration gradients away from the crust. In other words, the mass balance of Eq. (9) can be written in terms of a salinity flux

$$\mathbf{J}_S = U\mathbf{S} - \nabla S, \quad (8)$$

where  $\partial S/\partial \tau = -\nabla \cdot \mathbf{J}_S$ . At the surface,  $Z = 0$ , the upward water flux matches the evaporation rate, so  $U_Z = 1$ . The presence of a salt crust also sets  $S = 1$  there. As such, the salinity flux into the crust is given by

$$J_Z = 1 - \left. \frac{\partial S}{\partial Z} \right|_{Z=0}. \quad (9)$$

This flux vanishes,  $J_Z = 0$ , in the stationary solution  $S = \exp(Z)$ , although this scenario will still leave a constant upward flux of salt into the crust at whatever concentration is supplied by the reservoir, as we describe shortly. Variations in the near-surface salinity gradient will then modulate crust growth around this reference case. Where vertical gradients are strong, crust growth will be suppressed ( $J_Z < 0$ ), whereas over weaker gradients, crust growth will be enhanced ( $J_Z > 0$ ).

To demonstrate this modulation quantitatively, we calculate the surface salinity flux according to Eq. (9) in simulations at  $Ra = 100$ , with representative results for 2D shown in Fig. 5, and for 3D shown in Figs. 3(d) and 3(e). Supplemental Material Videos S2 and S3 [72] show the full dynamics of the two- and three-dimensional systems, respectively. Above downwellings plumes (2D) or sheets (3D), the salinity flux into the surface is positive and shows

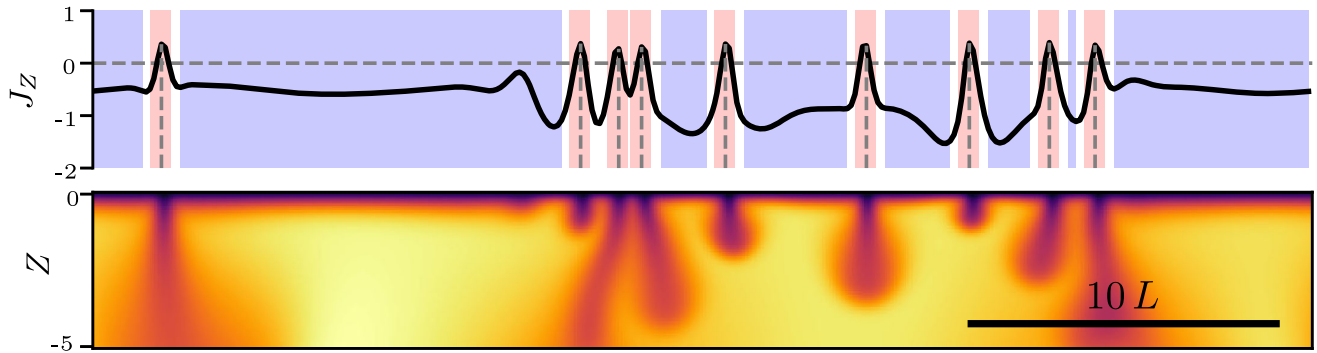


FIG. 5. Salinity flux ( $J_Z = 1 - \partial S/\partial Z$ ) into the modeled surface crust. The simulation snapshot is for  $Ra = 100$  at time  $\hat{\tau} = 150$ . Areas predicted to experience enhanced ( $J_Z > 0$ ) or suppressed ( $J_Z < 0$ ) salt flux are indicated as shaded red and blue areas, respectively. Peaks defined as local maxima with a flux value above zero are indicated as dashed lines and lie directly above downwelling plumes of high salinity; the lower panel gives the salinity  $S$  in the domain at the same time.

marked peaks, whereas between downwellings the salinity flux into the surface is negative, and roughly constant. As sketched in Fig. 2, this predicts the development of narrow regions of faster salt precipitation above any convective downwellings, which we argue gives rise to ridges there.

As visible in Videos S2 and S3 of the Supplemental Material [72], the positions of downwelling plumes slowly fluctuate as the simulations progress, as does the pattern of flux into the crust. The motion of the more well-established plumes is gradual, especially in 3D, but the presence of large ridges at some field sites suggests that feedback mechanisms may be needed to help stabilize the patterns over long periods of time. Such a feedback could act through a spatial modulation of the evaporation rate  $E$  based on salt coverage, which then acts to pin the position of the downwellings in space. We discuss how a feedback mechanism could work in more detail in Sec. IV E, with reference to observations of how the increased insulation of the thick ridges should reduce the evaporation rate near them [64].

We also note that the dynamics in a sufficiently deep lake should approach the case where the average surface salinity flux into the crust vanishes. This follows from the divergence theorem. For a deep lake, the descending plumes will mix diffusively with upwelling fluid over a timescale proportional to  $\Lambda^2$  for plume spacing  $\Lambda$ . Since the plumes start their fall from the surface at a characteristic velocity  $\mathcal{V}_B \sim \text{Ra}$  [64], this mixing will occur over depths of order  $\text{Ra}\Lambda^2$ . As they mix and lose buoyancy, the plumes will slow, setting a maximum depth that they can penetrate, of the same order. Below this depth, the average upward salinity flux of the flows from the reservoir must approach zero. Since in a statistically steady state the total salinity in the convecting part of the domain is constant, or fluctuating around a well-defined average value, the salinity flux into the surface must also approach zero. Probing this limit accurately, however, requires domain sizes well beyond the scope of our current simulations.

To make predictions of the crust dynamics at any particular field site, the salinity flux  $J_Z$  needs to be converted into estimates of the real salt flux into the crust. Assuming minimal volume change due to mixing, the density of the groundwater can be written as  $\rho = \rho_w + \beta c$ , where  $\rho_w$  is the density of pure water,  $c$  is the mass concentration of dissolved salts in the solution, and  $\beta$  is a coefficient of expansion. Analogous to the salinity flux in Eq. (8), the mass flux of salt, in dimensional variables, is

$$J_c = qc - D\phi\nabla c, \quad (10)$$

$$= qc_0 + \frac{\Delta\rho}{\beta} EJ_S, \quad (11)$$

where the second equation follows by changing variables using  $\rho = \rho_0 + S\Delta\rho$ . There is an offset between the two

fluxes, representing the fact that the groundwater feeding into the system from a distant source ( $S = 0$ ) contains some initial level of dissolved salt,  $c_0$ . In dimensional terms, the predicted salt mass flux into the crust is now

$$J_{c,z} = Ec_{\text{sat}} - D\phi\frac{\partial c}{\partial z}\Big|_{z=0}. \quad (12)$$

We apply this prediction to Owens Lake in Sec. IV C.

#### D. Model summary and predictions

The model of porous medium convection that is developed here can accurately predict much of the known phenomena of the crust patterns in dry salt lakes, as summarized in Sec. II. The driving mechanism of salinity-driven convection and its associated governing equations are drawn from existing models of salt lake dynamics [44,45,64] and observations of convection beneath tidal sabkhas [46,65], but we extend these models to consider interactions with the surface crust. Evaporation at the surface causes a vertical salinity gradient to emerge, which leads to salt precipitation and crust growth. If a critical Rayleigh number is surpassed, convective cells emerge and modulate the salinity flux into the surface, with faster precipitation expected over downwellings and slower crust growth over upwellings. We provide field observations in Sec. IV to quantify these predictions, and show that they are consistent with average growth rates on the order of millimeters per month, and about a twofold faster deposition of salt at downwellings relative to upwelling regions. Observing the pattern structure in 3D, we find that over sufficient time the downwelling features arrange into narrow sheets that delimit a closed polygonal pattern of convection cells. The scale of these polygons, in a steady state, does not have any strong dependence on the Rayleigh number. In particular, from  $\text{Ra} = 20$  to 1000 we show that the average wave number of the near-surface convection pattern changes by at most a factor of 4; the dominant wave number, which reflects the structure of the more stable, deeper convection cells, does not evolve significantly over this range and remains consistent with the critical wave number  $a_c = 0.76$ . These simulations predict that the pattern wavelength will be relatively insensitive to soil composition (which determines, e.g., permeability), groundwater chemistry (e.g., sulfate rich, or pure halite, affecting  $\Delta\rho$  and to a lesser extent  $D$ ), and robust to fluctuations in environmental driving parameters.

#### IV. EVIDENCE FOR CONVECTION AS A DRIVING MECHANISM

In Sec. II we outline a set of criteria against which to test mechanisms of pattern formation in salt playa. Briefly, any mechanism should be active in salt lake settings, modulate salt transport by directing more salt toward ridges, account

for the timescales of crust growth, explain the consistent wavelength of closed polygonal shapes in the crust, and be robust enough to explain all this across the variety of conditions associated with patterned crusts. Here, we explore these criteria in turn, focusing on empirical evidence from field work, supplemented by analog experiments. Details of field data collection are given in Appendix B, data processing in Appendixes C–H, and experimental methods in Appendix I. The results point toward convective overturning as a suitable driving mechanism of salt crust patterns.

### A. Convective instability

A driving mechanism should be specific to the geophysical conditions encountered in salt lakes. As our model is based on boundary conditions and governing equations of porous media transport that are appropriate for playa and sabkhas (e.g., Refs. [44,45,64,73,76]), we aim to prove here that typical dry salt lakes have conditions that would make them unstable to the onset of convective motion. To this end, we visited field sites at Owens Lake (California, USA), Badwater Basin (California, USA), and Sua Pan (Botswana) to show that they can be described by a Rayleigh number above the critical value of  $Ra_c \approx 14.35$  [43,64,73]. All sites show well-developed polygonal patterns, and details of the field methodology are given in Appendix B. These results are supplemented by experiments that visualize buoyancy-driven convective dynamics in conditions similar to those of real salt lakes (see Supplemental Material Video S4 [72]).

To determine the Rayleigh number appropriate for each field site, we measure the relevant parameters of Eq. (7). From grain-size distributions (data deposited in Ref. [81], analysis in Appendix C) we calculate  $d_s$ , the Sauter diameter [82], of near-surface soil samples. The results from  $4.3 \pm 0.6$  to  $138 \pm 23$   $\mu\text{m}$  represent a silt to fine sand. A high soil porosity  $\phi = 0.70 \pm 0.02$  was previously measured at Owens Lake [37]. From these, the relative permeability is estimated using the empirical relationship  $\kappa = 0.11\phi^{5.6}d_s^2$ , which fits a broad set of experimental and simulation data [83]. Across all sites  $\kappa = (3 \pm 2) \times 10^{-13}$  to  $(2.7 \pm 1.2) \times 10^{-10}$   $\text{m}^2$ . At Owens Lake, we also directly measure density differences of  $\Delta\rho = 210 \pm 10$   $\text{kg m}^{-3}$  between pore water samples taken from close to the surface and at approximately 1 m depth (data in Ref. [84]). The annual average evaporation rates of groundwater are taken as  $E = 0.4 \pm 0.1$  mm/day [29,37] for Owens Lake,  $0.3 \pm 0.1$  mm/day [38] for Badwater Basin, and  $E = 0.7 \pm 0.5$  mm/day for Sua Pan [35,39], with further details reviewed in Appendix D. These low levels of groundwater evaporation are characteristic of salt pan environments, and similar rates are seen in active playa of the Atacama desert ( $E = 0.5 \pm 0.1$  mm/day [40]) and sabkhas near Abu Dhabi ( $E = 0.2 \pm 0.05$  mm/day [41]). Finally, we assume the dynamic viscosity of the groundwater to be a constant

$\mu = 10^{-3}$  Pa s. A detailed description of the datasets from Owens Lake and Badwater Basin is in Ref. [11].

From these observations, we calculate  $Ra$  at 21 sites around Owens Lake, five in Badwater Basin, and seven at Sua Pan. The median values at these three regions are  $Ra = 3700$ ,  $36\,000$ , and  $420$ , respectively. The values for all 33 sample locations are between  $Ra = 120 \pm 50$  and  $(1.2 \pm 0.5) \times 10^5$ , well above  $Ra_c$ . The Sauter diameters, permeabilities, and Rayleigh numbers for all sites are given in Table IV. The conditions throughout these patterned salt playa are therefore suitable to expect a convective overturning of their groundwater, with plumes of high salinity sinking downward from the surface.

It is interesting to note that convective plumes of salt-rich water have also been observed by electrical resistivity measurements after a heavy rainfall on salt crusts near Abu Dhabi [46] and beneath wind-tidal flats in Texas [65]. While these are slightly different phenomena, involving the sudden addition of salt-rich brine to the surface as the rain dissolves salt, they demonstrate convection in similar geophysical conditions to salt lakes. The Rayleigh numbers calculated for these two cases are up to about  $40\,000$  and  $90$ , respectively [46,65].

We complement these observations with analog experiments in Hele-Shaw cells to demonstrate buoyancy-driven convection in porous media under conditions comparable to the field. These experiments are inspired by Refs. [85–87], but instead of using a narrow and empty gap between the cell walls to create the porous medium, we use a 0.8-cm-thick cell filled with glass beads. We apply a strong surface evaporation driven by heat lamps and ventilation, and the base of the cells is connected to fluid reservoirs with a fixed salt concentration of  $50$   $\text{kg m}^{-3}$ . Further details of the experimental methods are given in Appendix I, and Supplemental Material Video S4 [72] is an example time-lapse video of an experiment in progress. To observe whether a convective instability arises for different conditions, we systematically vary the grain sizes of the glass beads. This modifies the relative permeability of the system and allows us to change the Rayleigh number of the experiments. Convection is seen in all experiments above  $Ra_c$  but not in the finest-grained case, where  $Ra \ll Ra_c$ . These results are consistent with those of Wooding *et al.* [85], who experimentally confirmed theoretical predictions of the onset of convection for the slightly different case of a salt lake with surface ponding, or constant pressure boundary conditions. Finally, we note that the range over which the experiments show convection, between  $Ra = 20 \pm 10$  and  $(1.3 \pm 0.3) \times 10^3$ , also coincides with much of the range of Rayleigh numbers that we estimate from the field sites.

### B. Mapping salt heterogeneity

If salt polygon growth is driven by convective dynamics happening beneath the surface, then horizontal differences

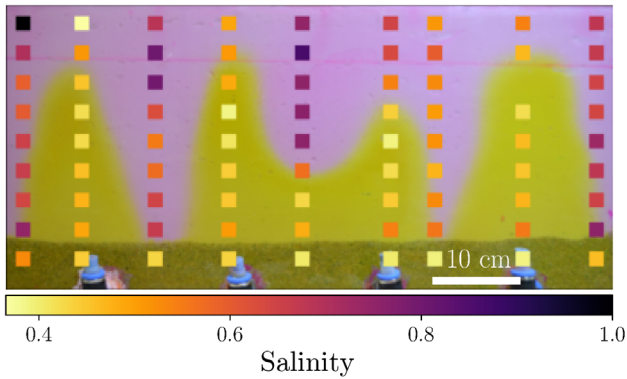


FIG. 6. Convective plumes in an experimental Hele-Shaw cell are highlighted by dye (the brighter upwelling fluid results from dyeing the reservoir, well after convection sets in). The motion is coupled to the salinity, which is measured at the colored squares by destructive sampling.

in salt concentration should be detectable in soil and pore fluid under typical field conditions, and also in laboratory-based analog experiments. Salt variations of this nature have been seen in sabkhas after rain [46,65]. We provide evidence here of salt-rich plumes beneath the crust of Owens Lake and show that the plumes are correlated with the positions of the ridges in the crust.

First, to demonstrate the coupling of salt concentration and convective motion under controlled conditions, we sample one of the Hele-Shaw experiments introduced in Sec. IV A. For this, we dissect an experiment that is undergoing convection, and which has been evolving under constant conditions for two months. Samples are extracted from locations along the downwelling and upwelling plumes, as indicated by the motion of dye added into the reservoir fluid a few days before sampling. As shown in Fig. 6, the fluid flow in the analog experiments is clearly driven by, and coupled to, variations in salinity. Pore water samples taken from the upwelling regions (dyed yellow in the figure) show systematically lower salinity than those taken from downwellings.

Next, from the field we collect samples of wet soil from fresh trenches dug at two unmanaged sites at Owens Lake. Surveys of the surface relief are made before sampling, using a terrestrial laser scanner (TLS; see Appendix E and Ref. [22] for methodology; data deposited in Ref. [88]). These show the presence of salt polygons of about 2 m in size delimited by high ridges, as in Fig. 7(a). In each case, we sample soil along a grid pattern in a cross section below a polygon, including beneath two bounding ridges. Analysis of the salt concentration of the samples with respect to pore water content shows direct evidence of plumes of

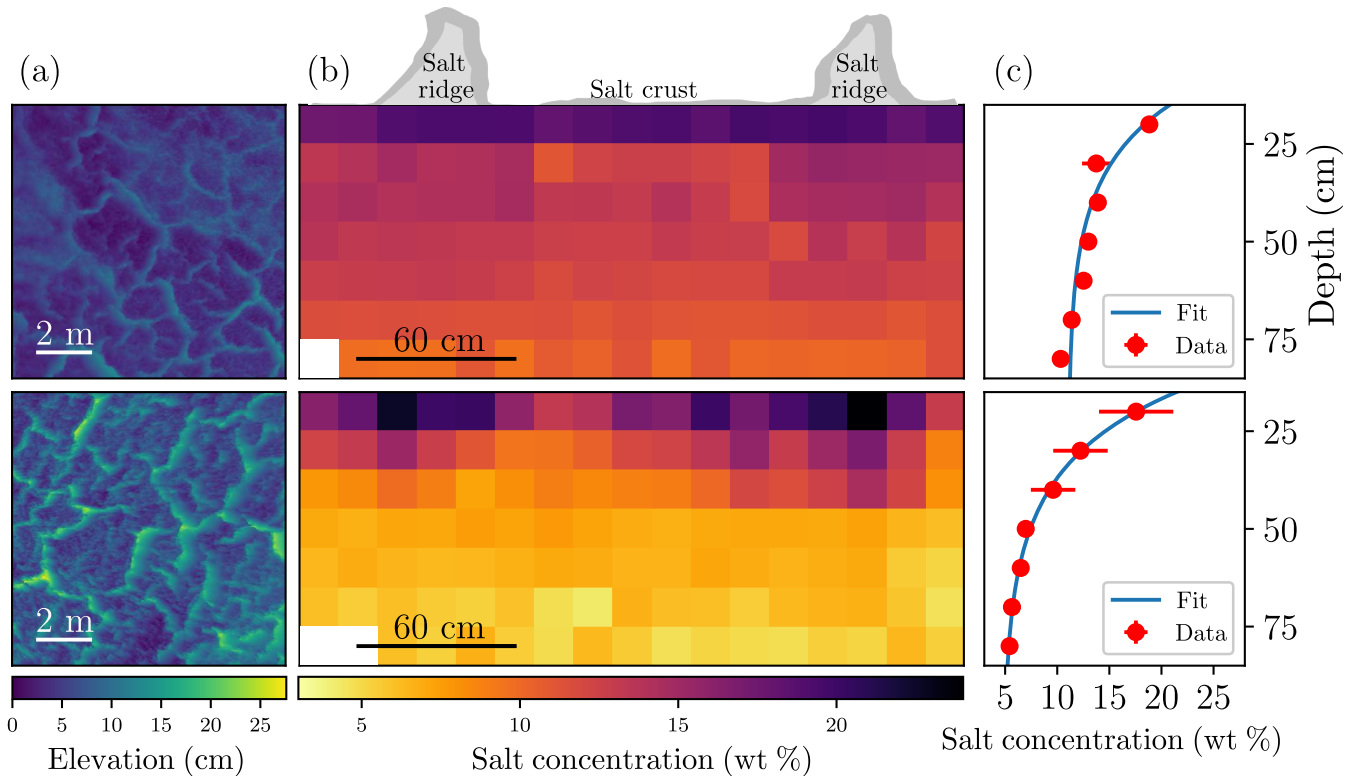


FIG. 7. Surface height maps and subsurface salinity profiles for two sites (site 1, top; site 2, bottom) at Owens Lake. (a) TLS scans give the elevation of ridges on the surface crust. (b) Cross sections of polygons at Owens Lake show the variation of salt concentration with depth and relative to the ridge positions. Each square corresponds to the salt concentration in the pore fluid of an individual field sample. (c) Exponential fits (see Appendix H) are made to the changing salt concentration with depth. Red dots represent horizontally averaged salt concentrations from data in (b), and error bars show the standard deviation.

high-salinity fluid below the salt ridges [Fig. 7(b), methods in Appendix F, and data deposited in Ref. [89]]. Specifically, we test whether the distribution of salt concentrations in an area below each ridge is different from that below the flat pan of the polygon; testing this hypothesis via the two-sample Kolmogorov–Smirnov (KS) test shows that the distributions below ridges and flat crust are statistically distinct ( $p < 0.02$ ) at both sites.

The measurements of the salt concentration in the pore water also show an exponential decay in salinity with depth [Fig. 7(c)] consistent with a salt-rich boundary layer that is heavy enough to drive convection in a porous medium. As evidence for this, we recover representative values for the boundary layer thickness from exponential fits to the horizontally averaged salt concentrations at both trench sites (see Appendix H). The observed values of  $13.5 \pm 5.3$  and  $17.7 \pm 1.5$  cm are comparable to the natural length scale of  $L = \varphi D/E = 15.1 \pm 8.0$  cm estimated for Owens Lake. Thus, not only does direct field sampling of groundwater beneath a patterned salt crust show both horizontal and vertical variations in salt concentration, which support the hypothesis that the system is unstable and convecting, but it also demonstrates that the plumes of high salinity are colocalized with the surface ridges.

### C. Surface salt flux in the field

A driving mechanism for pattern formation should be able to spatially modulate salt transport to the soil surface, leading to salt ridge growth on a scale of months. We demonstrate this growth at Owens Lake through a time-lapse video (Supplemental Material Video S1 [72]), which shows the surface crust dynamics over a period of approximately four months in spring 2018. At Sua Pan, crust dynamics have been measured by TLS scanning of several sites over the course of several months [15]. Active crusts there showed average growth rates of 0.7 to 1.5 mm/month. The fastest short-term growth rates of ridge features, briefly reaching up to 10 mm/month, were associated with ridge thrusting. In Sec. III C, we explore the corresponding predictions of our model. Specifically, Eq. (12) describes the expected salt flux into the surface, depending on the salt concentration gradient there. Here, we apply the framework of this model to the maps of the subsurface salt concentration measured at Owens Lake (Fig. 7). In particular, we show that the observed variations are sufficient to drive average crust growth rates on the order of millimeters per month along with a preferential growth of the ridges over the rest of the crust.

To calculate the expected salt flux into the surface, we estimate the near-surface gradient in salt concentration from the field data from our trench sites. Dividing this data between regions beneath the ridges and centers of each polygon, we use an exponential fit to recover the effective thickness of the salt-rich boundary layer  $L'$ , the background salt concentration  $c_{\text{bkg}}$ , and the salt

TABLE I. Salt flux into the surface  $J_{c,z}$  and crust growth rate  $r$  inferred at the polygon ridges and centers for the two sites at Owens Lake depicted in Fig. 7. The error bounds consider independent sources of uncertainty, while the values in parentheses give ranges taking into account all sources of uncertainty (i.e., including lakewide uncertainties in  $E$ ,  $D$ , and  $\varphi$ ).

Site	Area	$J_{c,z}$ ( $10^{-7}$ kg m $^{-2}$ s $^{-1}$ )	$r$ (mm/month)
1	Ridge 1	$5.6 \pm 2.0(3.9)$	$1.5 \pm 0.6(1.1)$
1	Ridge 2	$6.8 \pm 1.2(3.2)$	$1.8 \pm 0.4(0.9)$
1	Center	$3.3 \pm 2.5(4.9)$	$0.9 \pm 0.7(1.4)$
2	Ridge 1	$5.3 \pm 1.3(3.8)$	$1.4 \pm 0.4(1.1)$
2	Ridge 2	$6.8 \pm 1.1(3.1)$	$1.8 \pm 0.3(0.9)$
2	Center	$2.1 \pm 0.9(4.8)$	$0.6 \pm 0.3(1.3)$

concentration at the surface  $c_{\text{sat}}$  for each such region. For this, the weight fractions of salt are rescaled by the densities of standard salt solutions to give concentrations  $c$  in terms of the mass of dissolved salt per unit volume of fluid. Further details of the fitting are given in Appendix H.

Substituting the exponential form of the fit into Eq. (12) yields a prediction for the mass flux of salt, in terms of measurable quantities, of

$$J_{c,z} = E c_{\text{sat}} - \varphi D \frac{c_{\text{sat}} - c_{\text{bkg}}}{L'}. \quad (13)$$

The values for  $L'$  and  $c_{\text{bkg}}$  below each ridge and polygon center are extracted from the fits. For  $c_{\text{sat}}$ , the fitted values are all consistent with each other, so a common value of a saturated solution  $c_{\text{sat}} = 316$  kg m $^{-3}$  is used to minimize uncertainties. As in Sec. IV A, we use values for the evaporation rate  $E = 4.6 \times 10^{-9}$  m s $^{-1}$  and porosity  $\varphi = 0.7$  taken from previous observations at Owens Lake [29,37]. For an effective diffusion constant, we use the tortuosity-corrected diffusivity  $D = 1.00 \times 10^{-9}$  m $^2$  s $^{-1}$  (see Appendix G). Finally, we measure the density of salt crust samples collected from Owens Lake to be  $\rho_{\text{crust}} = (960 \pm 50)$  kg m $^{-3}$ . This value is used to convert mass flux rates into crust growth rates.

The resulting salt flux and growth rates for the ridges and centers of the two trench sites from Fig. 7 are shown in Table I. The derived salt flux into the surface is about twice as high at the ridges, as compared to the centers of the polygons. To allow for a clear statistical comparison between these rates, only independent sources of errors are propagated (i.e., excluding uncertainties in  $E$ ,  $D$ , and  $\varphi$ , as these will affect all rates in the same way) to give the main uncertainties reported in Table I. Within these uncertainties, we see a consistent difference between crust growth rates at polygon ridges and centers. As salt is being added faster to the ridge areas, we expect differential growth focused on the ridges. Although the crust morphology can become quite complex [12,19,90], the faster expansion of the crust in these locations can plausibly

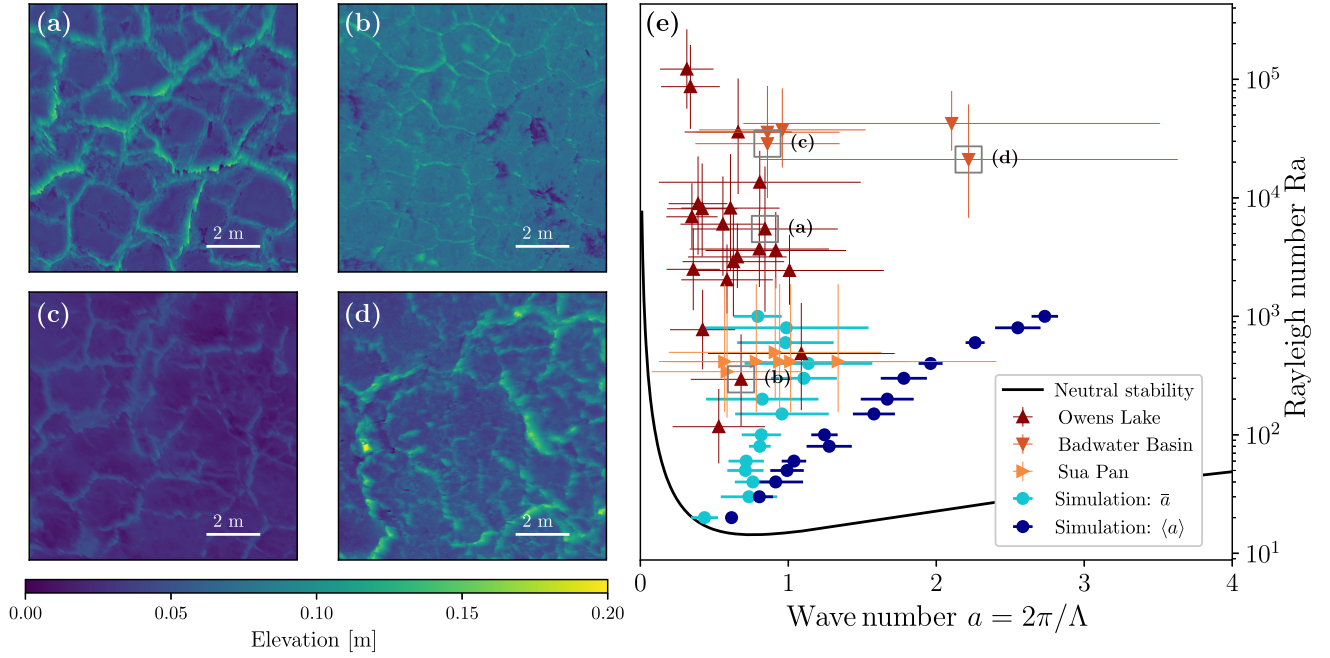


FIG. 8. Field observations of the length-scale selection of salt polygons. Panels (a)–(d) show the surface relief recorded at several field sites. Panel (e) maps data from the field onto the stability diagram of porous media convection in a salt pan. The neutral stability curve (black line) is the theoretical boundary above which an evaporating stratified pore fluid is unstable to perturbations of wave number  $a$ . Various triangles show measurements at Owens Lake, Badwater Basin, and Sua Pan, with letters indicating data from the sites in panels (a)–(d). Turquoise and blue dots show the average and dominant wave number measured in simulations, respectively (data from Fig. 4).

contribute to differential strains, and features like ridge thrusting or local buckling. This is consistent with the faster dynamics seen at ridges in Sua Pan [15] and that we report at Owens Lake (see Supplemental Material Video S1 [72]).

Over long times, the average crust growth rate will be essentially constrained by the evaporation rate and the amount of salt in the groundwater feeding into the lake. However, it would not be surprising if these rates vary with time, e.g., seasonally, or via extreme events like surface flooding. As we do not account for the excess mass of the hydrated states of any of the crust materials (especially mirabilite present as a significant minority species of salt at Owens Lake and Sua Pan, although not noticeably present at other pans, such as Badwater Basin), the rates we report in Table I also represent a lower bound on the anticipated crust growth rates.

In summary, the heterogeneous salinity distribution measured below salt polygons in the field infers variations in the salt flux to the surface if the subsurface fluids are undergoing porous medium convection. Within the framework of our convection model, the measured pattern of salt concentration near the surface of the crust implies about a twofold increase in crust growth rate at the ridges, versus the centers of salt polygons. The predicted crust growth rates on the order of millimeters per month are also consistent with the timescale of crust growth observed in the field, which shows that noticeable changes can occur over months.

#### D. Pattern length scale

If groundwater convection leads to preferential locations for salt precipitation, and from thence to salt crust patterning, then the convective cells and crust polygons should have similar length scales and patterns. We present model predictions for the length-scale selection of convection in Sec. III B. To test these predictions in the field, we measure the surface relief of the crusts at multiple sites from all three dry lakes using a terrestrial laser scanner (see Appendix B). The crusts display the typical polygonal patterns of salt lakes, as shown in Figs. 8(a)–8(d), with further data in Refs. [11,15]. From each scan we extract a characteristic wavelength for the pattern, based on the dominant frequency of the power spectrum, using the methods reported in Ref. [15]. Full results are given in Table IV. In all cases, the pattern wavelengths range from  $\lambda = 0.53 \pm 0.20$  to  $3.02 \pm 1.40$  m. These are converted into dimensionless wave numbers  $a = 2\pi L/\lambda$  using the characteristic length scale  $L = \varphi D/E$  as calculated for each lake ( $E$  from Sec. IV A,  $\varphi$  and  $D$  from Sec. IV C). The results are summarized in Fig. 8(e), which shows the Rayleigh number and wave number for each site studied. A direct comparison of the pattern wave number and evaporation rate is given in the appendixes.

We find that the wave numbers characterizing the surface crust patterns in the field are clustered near the critical wave number for convection  $a_c = 0.76$  and largely independent

of  $Ra$ . In Sec. III B, we predict how the statistically steady state of subsurface convection should look. In this state, the average wave number increases slowly with  $Ra$  by about a factor of 4 from  $Ra = 20$  to 1000. This is attributed to the proliferation of small, transient features superimposed on more stable convection cells. The dominant wave number given by the peak or mode of the power spectrum shows little to no dependence on  $Ra$  and is argued to better represent the long-term behavior of the convection cells. As shown in Fig. 8(e), although there is large scatter in the data, the wavelengths of the crust pattern broadly match the wavelengths of the dominant features of the subsurface convection expected in a statistically steady state.

Furthermore, for the field sites there should be ample time for the convective dynamics to develop toward the steady-state condition. In the model, the timescale most appropriate to characterize the dynamics of convection is  $T/\epsilon$ , where  $T = \varphi^2 D/E^2$  describes how the boundary layer will develop in the absence of convection, and  $\epsilon = (Ra - Ra_c)/Ra_c$  accounts for the increased vigor of convective motion as the driving forces increase (see also Ref. [64]). For the relevant parameter values of Owens Lake,  $T/\epsilon$  is just over one day. Alternatively put, one year of evolution at Owens Lake, for a site with a representative value of  $Ra = 3700$ , would represent a rescaled time of  $\hat{\tau} = 350$ . This is long compared to the timescale of  $\hat{\tau} = 30$  that we use to characterize the steady-state conditions in Figs. 4 and 8.

Finally, as shown in Figs. 8(a)–8(d), polygon ridges are relatively narrow features. To characterize their size, we thresholded our surface relief maps using Otsu’s method [91]. The relative area occupied by ridges measured in this way is  $24 \pm 8\%$  (mean  $\pm$  standard deviation); this may be a slight overestimate, due to occlusion of the TLS line of sight behind larger ridges. In the 3D simulations, the comparable features are downwellings, which we characterize as areas of positive surface salinity flux at  $\hat{\tau} = 30$ . These cover 11%–18% of the surface; narrower features are seen at higher  $Ra$ , but the range of  $Ra$  explored is small. Although the salt ridges can be relatively complex, involving breaking and thrusting for example, the convective model qualitatively captures the essential asymmetry between the narrow ridge features and the flat pans between them.

In summary, the pattern wavelength we measure for salt polygons at a range of sites across three different salt lakes is found to be consistent with the length scale expected for buoyancy-driven convection going on in a statistically steady state. Simulations of the dynamics in a three-dimensional domain [see Fig. 3(d)] also show that the convective mechanism can produce patterns of closed polygonal shapes at this length scale. These patterns are qualitatively similar to the salt polygons observed in the field [Figs. 8(a)–8(d)] with relatively narrow features delimiting the larger polygonal shapes.

## E. Environmental variation and remaining challenges

To this point, we have focused on the effects of varying environmental conditions as they contribute to the Rayleigh number and natural length scale of the convection problem. We showed that a wide range of measured field conditions should lead to convection and to convection cells with a size and pattern that is consistent with the observed surface crust patterns; faster crust growth and thicker accumulations in ridges is shown to correlate with the downwellings of the subsurface convection. In this section, we briefly look at and discuss other factors, including the salt chemistry, crust thickness, and features like cracks and crust wrinkling. We also discuss some of the remaining assumptions and challenges of the convective model in explaining crust patterning.

In addition to the soil, we characterize the composition of the salt crust at Owens Lake and Badwater Basin (see Appendix G for methods; data deposited in Ref. [84]). Both sites are predominantly halite, although Owens Lake additionally has significant concentrations of carbonates and sulfates [37,84]. Between all the field sites, we also observe salt crusts with thicknesses from below a centimeter to approximately 30 cm. Across these differences in soil and salt crust composition there is a similar appearance

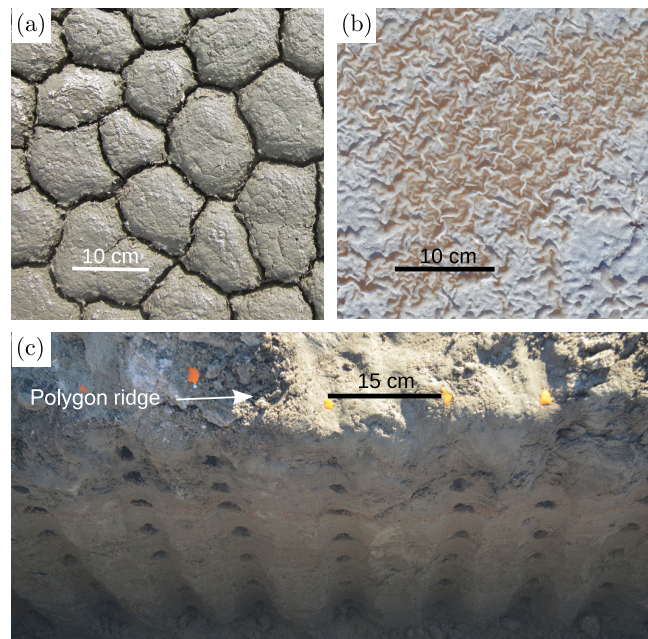


FIG. 9. Additional surface and subsurface features at Owens Lake. (a) Small-scale hexagonal mud cracks can be seen in the soil about 10 m away from one of our field sites. (b) Wrinkles are also observed in the salt crust adjacent to one of the polygons that serves as a field site. (c) At a trench site, the soil layering is exposed. The surface position of a polygon ridge is indicated by the white arrow, and holes mark the sampling locations. The horizons in the soil beneath the polygon are visible and undisturbed (see, for example, the reddish layer near the third sampling hole from the top).

of the salt polygons. This agrees with a mechanism like subsurface convection, which is relatively insensitive to salt chemistry. It will, conversely, present difficulties to any mechanism that is reliant on specific salts, such as mirabilite, or which varies strongly with crust thickness.

Other surface features, including cracks and wrinkling or buckling, are also associated with salt crusts [12,17]. While studying Owens Lake, we observe well-ordered hexagonal desiccation cracks in crust-free mud with approximately 10-cm spacing, as shown in Fig. 9(a). These appear at the crust-free edge of a pan that is otherwise covered in salt ridges (with a spacing of 1–2 m). The hexagonal crack patterns can be explained as the result of the intermittent and episodic cracking of the soil, as water levels fluctuate [51]. However, they form at a very different scale from the salt ridges, and the cracks develop as localized depressions in the ground, rather than upthrust ridges. Further, despite their presence near the salt crust, there are no signs of preferential precipitation of salt in the cracks. We also observe surface buckling of the salt crust at Owens Lake, as shown in Fig. 9(b) (see also Supplemental Material Video S1 [72] on dates May 7 through May 11, 2018). These features appear when the crust is solidifying and may result from the stresses induced by phase changes or the addition of salt mass into the crust. However, the scale of their features is, again, much smaller than those of the dominant polygonal ridges in the crust, and the patterns formed are also different. Finally, we note that throughout our core samples and trench sites, as in Fig. 9(c), the soil horizons remain normal and undisturbed by the presence of surface ridges. This would not be the case if deep fractures were occurring along with the ridge formation (as in, e.g., ice-wedge formation in permafrost terrain [48]).

More generally, we treat the salt crust as two dimensional surface, of nominal thickness. This is a necessary simplification, given the novelty of the hypothesis advanced here. However, there will be some internal dynamics within the salt crust itself, beyond the scope of our model. For example, dissolution will be favored at the base of the crust in contact with groundwater, and precipitation at the top where evaporation occurs. Similar observations have been made in playa [90] and in lab [92,93] studies of efflorescence with cultural heritage applications. Dissolution-precipitation dynamics raises porosity in crusts, leading to a “fluffy” texture, trapped air pockets, self-lifting effects [90,92,93], hollow shells left by evaporating droplets [94], and a lower threshold for dust entrainment [24]. We account for the high crust porosity while calculating growth rates in Sec. IV C, but a more nuanced approach may give further insight, including into dust models.

There is also likely to be an element of positive feedback between the growth of the salt crust and the dynamics of the convective plumes. Our simulations show that, without such a feedback, the positions of downwelling features slowly fluctuate in space, although this tendency is weaker

in 3D than in the 2D simulations. A feedback cycle, where evaporation rates are affected locally by the presence of the ridges, can act to stabilize the locations of the plumes. This has been demonstrated [64] by simulations in which downwellings tend to move toward, and stay at, locations with lower evaporation rates. We also measure temperature and relative humidity records from Owens Lake [64], which show that evaporation rates should be slower at the ridges compared to the centers of polygons, in a way consistent with such a feedback mechanism. Further model development along these lines would be promising.

Incorporating feedback into crust evaporation may also help refine predictions of wavelength selection. The scale of salt polygons matches the dominant wavelength of our simulations, which we argue to be a representative measure of a long-time integration of the more stable convection pattern. The effect of the smaller-scale, transient microplumes remains uncertain. As captured by the average wave number, these are more prevalent at higher Ra, but their faster dynamics (changing visibly over simulation times of 0.1, or about two weeks in real terms) mean that they should only contribute weakly to the surface pattern, which develops over months. This prediction can be checked in simulations that modulate surface evaporation, based on tracking of the total amount of salt accumulating at the surface over time.

As a final point, one may also consider thermal contributions to buoyancy, and phenomena like double-diffusive convection. A typical 10 °C diurnal variation [64] will change water density by about  $\Delta\rho_T = 1 \text{ kg m}^{-3}$  compared to the  $\Delta\rho_S \simeq 200 \text{ kg m}^{-3}$  density contrast due to solutes at Owens Lake. The buoyancy ratio  $N = \Delta\rho_S/\Delta\rho_T \simeq 200$  means that the driving forces and speeds of thermally driven flows will be reduced by a factor of  $1/N$  compared to solute-driven flows (see, e.g., Ref. [95] for review of double-diffusive flow in porous media). Such effects can therefore be assumed to be negligible.

## V. DISCUSSION AND CONCLUSION

Salt deserts, playa, and pans are common landforms important to climate balances of dust, energy, and water, and express a rich repertoire of patterns and dynamics. Here we show that, in order to model and understand the surface expression of such deserts, insight is gained by considering the crust together with the subsurface dynamics. In particular, we show how the emergence of regular salt polygons, which are a common salt crust pattern, can result from their coupling to a convection process in the soil beneath them. The existence of salinity-driven convection in salt pans is itself already an anticipated finding (see, e.g., Ref. [44]). Furthermore, a salinity gradient below the surface, strong enough to drive such a convection, has been measured at Owen’s Lake [37] and strong horizontal salinity gradients indicative of convective motion have been shown to exist in

sabkhas [46,65]. What we demonstrate is that this convection process develops into a statistically steady state characterized by large-scale convection cells with a wavelength of a few meters after a few weeks of evolution under typical field conditions. We further show how this can explain the remarkably consistent appearance, growth rates, polygonal shape, narrow ridges, and representative wavelengths of the salt crust patterns observed in different parts of the world, including our field sites at Sua Pan, Badwater Basin, and Owens Lake.

Our findings help to elucidate the relationships between subsurface drivers and the development of surface crust patterns. Better knowledge of crust development can improve dust emission models [7,24,31], including quantifying the connection of salt pan hydrology to controls on dust emission [33] such as those used at Owens Lake [29,30]. As further context, dusts and aerosols remain one of the larger uncertainties in modeling climate sensitivity [96] with, e.g., feedback from soil biocrust degradation recently predicted to contribute half as much as direct anthropogenic aerosol emissions by 2070 [97]. While the surface variability of crusted surfaces can be probed using remote sensing [23], our model is a first step to improving predictions of how subsurface hydrologic variability links to surface crust variability. This knowledge is increasingly important as saline lakes like the Dead Sea or Great Salt Lake are shrinking [98], and their newly exposed beaches are candidate areas for salt crust formation and dust emission.

To establish the connection between surface features and subsurface flows, we demonstrate consistent results from theoretical and numerical modeling, analog experiments, and field studies. In contrast to previous explanations of crust patterns [12,17], this model is able to explain the robustness of the pattern length scale by considering the statistically steady state of porous media convection, based only on measured environmental parameters. In fully three-dimensional simulations, the convective dynamics are also shown to give rise to closed-form polygonal shapes. More importantly, the model is able to predict a suite of quantitative details, such as the timescales required for convection to set in, the rates of crust and ridge growth, the positions of the ridges above salt-rich plumes, and the relative narrowness of the ridge features. At the downwellings, the salinity is higher, and therefore, the salinity gradient between the crust and the underlying fluid is weaker (compare sketch of Fig. 2 to measurements in Fig. 7). As salt transport is a balance of advective and diffusive processes, this will lead to an increased rate of salt precipitation above downwelling features, contributing to the growth of ridges at the boundaries of convection cells. After the initial emergence of ridges, the growth process might be bolstered by feedback mechanisms such as a modulation of the evaporation rate by the presence of ridges, cracks, or surface wicking phenomena.

As such, our results show how salt polygons are part of a growing list of geophysical phenomena, such as fairy circles [99], ice wedges [49], polygonal terrain [50], and columnar joints [51], which can be successfully explained as the result of the instability of a dynamical process.

Data of soil sizes [81], surface maps [88], salt chemistry [84], groundwater salinity [89], and field site images [100] are available at PANGAEA. 2D simulation code is available at Zenodo [101]. Scripts, data, and images to reproduce all figures in this work are available in Ref. [102].

## ACKNOWLEDGMENTS

We thank Grace Holder (Great Basin Unified Air Pollution Control District) for support at Owens Lake, the U.S. National Park Service for access to Death Valley (Permit No. DEVA-2016-SCI-0034), and Antoine Fourrière and Birte Thiede for their work on preliminary experiments on convection. TLS processing used the Iridis Southampton Computing Facility. The 3D numerical simulations were carried out on ARC4, part of the High Performance Computing facilities at the University of Leeds, United Kingdom. M. R. T. was supported by the Leeds-York-Hull Natural Environment Research Council Doctoral Training Partnership Panorama under Grant No. NE/S007458/1. Sua Pan work was funded by Natural Environment Research Council (Grant No. NE/H021841/1), World University Network, and Southampton Strategic Interdisciplinary Research Development Funds, and enabled by Botswana Ministry of Environment, Wildlife, and Tourism (Permit No. EWT 8/36/4 XIV) and Botswana Ash (Pty) Ltd.

J. L., M. E., and L. G. wrote the original draft of the manuscript; all authors reviewed the manuscript. J. L. participated in fieldwork at Owens Lake and Badwater Basin, analyzed the soil salinity and grain size distributions, performed numerical experiments of the 2D simulation, performed the Hele-Shaw experiments, analyzed all data except for the 3D simulations and TLS measurements, and created the data visualizations. J. M. N. participated in fieldwork at Owens Lake, Badwater Basin, and Sua Pan and performed and analyzed the TLS measurements. M. E. developed the theory of convective dynamics and programmed the 2D simulation. V. K. performed the x-ray analysis, supervised J. L. on the grain size measurements, and provided feedback for the soil composition and salt species analysis. G. F. S. W. participated in fieldwork at Sua Pan. M. R. T. performed numerical experiments and analyzed the data from the 3D simulations. C. B. supervised M. R. T., programmed the 3D simulation, and provided feedback for the theoretical model. L. G. conceptualized the study, developed the theory of convective dynamics, supervised J. L. and M. E., performed the water density measurements, and participated in fieldwork at Owens Lake and Badwater Basin.

**APPENDIX A: NUMERICAL SIMULATION**

The 3D simulations use a pseudo-spectral element method where the horizontal directions, over which the numerical domain is periodic, are treated using fast Fourier transforms, and the vertical (bounded) direction is decomposed into elements, each of which is treated using Gauss-Lobatto-Legendre quadratures (see, e.g., Ref. [103]). The time derivative is approximated using a second-order backward differentiation formula, and the nonlinear term is extrapolated using a Taylor expansion of second order. The coefficients of the resulting schemes can be found in Ref. [104]. All simulations are carried out on a domain of depth 10 and horizontal area of  $24\pi \times 24\pi$ . Pattern wave numbers are calculated as in [68], as

$$\langle a \rangle = \frac{\int kP(k)dk}{\int P(k)dk},$$

for wave numbers  $k$  calculated in the horizontal plane, and where  $P(k)$  is the radially-averaged power spectrum for the salinity field at the gridpoints closest to depth  $Z = 1$ .

For the 2D simulations of wave-number selection (Fig. 4), we use the same numerical solver and impose the solution invariance in one of the horizontal directions. These simulations have horizontal domain size  $12\pi$  and depth 10 or 20. Pattern wave numbers are calculated from the salinity at the grid point closest to  $Z = 1$  as in 3D, but without radially averaging the power spectra. The dominant wave number is identified as the mode with the highest power spectral density. All other 2D simulations are carried out using a stream-function-vorticity approach based on Refs. [105,106] with a detailed implementation described in Ref. [64].

**APPENDIX B: FIELD DATA COLLECTION**

Field work is conducted at Owens Lake and Badwater Basin in November 2016 and January 2018; see, e.g., Refs. [107,108] for geological descriptions of the area. The Owens Lake sampling sites are indicated in Fig. 10. At Badwater Basin, five sites are visited approximately 500 m south of the main tourist entrance to the playa. For both locations, field methodology and data collection are fully documented in a separate data description publication [11].

At Owens Lake, we use field site labels referring to surface management cells of the dust control project there [109]. These labels link either to managed cells or to unmanaged areas in the direct vicinity of a managed cell. Labels typically start with “TX-Y,” where X is a number and Y is a number or letter. The first number refers to the water outlet taps along the main water pipeline that crosses the lakebed south to north and is used to irrigate management cells. The numbers and letters after the hyphen refer to subregions branching from the same tap. For some sites we investigate more than one polygon. This is indicated with

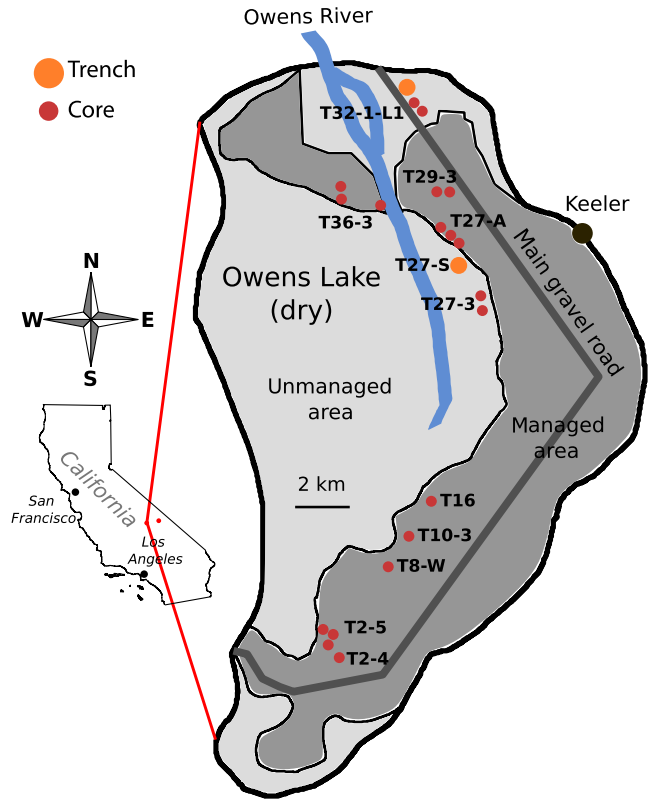


FIG. 10. Schematic map of Owens Lake (California, USA) with locations of soil core (red) and trench (orange) sites marked. Labels give the names of local dust management areas.

brackets; e.g., T27-A (3) is the third polygon investigated at site T27-A, which corresponds to the addition (A) region of the management cell next to the 27th tap. Bracketed numbers are used for the sites visited at Badwater Basin.

To evaluate the profile of salt concentration below polygons, at most sites, soil cores (4-cm Dutch gouge auger) are taken to a depth of up to 1 m. The soil shows normal bedding [see also Fig. 9(c)] indicative of sedimentation following flooding. Samples are collected from each visible soil horizon, or with a vertical resolution of  $\Delta z = 10\text{--}15$  cm.

Trenches are also dug at sites T27-S (site 1 in Figs. 7 and 12) and T32-1-L1 (3) (site 2) in order to take samples along cross sections below salt polygons. The trenches are dug about 200 cm in length, 40 cm in width, and down to a water table of approximately 70 cm. Soil samples are taken from a freshly cleaned trench wall in a grid pattern with spacings of  $\Delta x = 15$  cm and  $\Delta z = 10$  cm. An example of such a trench along with sampling locations is shown in Fig. 9(c). The samples have an average volume of approximately 10 ml and are taken using a metal spatula, which is cleaned with distilled water and dried before each use. The samples are a mixture of soil with a grain size of medium sand to clay, water, and salt (both dissolved and precipitated). After collection, samples are immediately stored in airtight containers, which are sealed with parafilm.

To evaluate the density difference  $\Delta\rho$ , we collect pore water samples at Owens Lake from eight sites, including liquid taken from directly below the surface (in cases where the water table is at or within 10 cm of the surface) and at a depth of about 1 m.

Samples from Sua Pan are collected during a different field campaign reported in Ref. [15]; site labeling follows that publication. Sediment samples at Sua Pan are collected 2 cm below the crust in August 2012. These are double bagged and subjected to grain size analysis only.

At all three dry lakes, surface height maps are collected with a Leica TLS; a P20 model is used at Owens Lake and Badwater, and a ScanStation at Sua Pan. The scanner head is positioned at least 2 m above the playa surface, and scans are performed before the surface is disturbed by sampling.

GPS locations of all sites are provided in Table IV.

### APPENDIX C: SOIL CHARACTERIZATION

Soil samples from Owens Lake, Badwater Basin, and Sua Pan are analyzed to determine their distribution of grain sizes. This analysis is performed using the soil remaining after a sample's salinity is determined (Appendix F). Soil grain size distributions are measured by laser particle sizer (Coulter LS 13 320), from which the Sauter diameter (the mean diameter, respecting the soil's specific surface area [82]) is calculated. For each site, a representative  $d_S$  is calculated as the average Sauter diameter of all soil samples (for trenches, one sample per depth) from that site. For Sua Pan, only samples from sites B7 and L5 are available;  $d_S$  for the other five sites is estimated as the mean of the measured values at these two sites. All grain size data are deposited in Ref. [81].

Soil porosity has previously been measured to be around  $\phi \approx 0.70 \pm 0.02$  [37] at Owens Lake. Because of lack of similar measurements at Badwater Basin and Sua Pan, we use the value measured at Owens Lake for the calculations of  $\kappa$  and Ra at these sites. For each site, a permeability is then calculated based on the Sauter diameter and porosity as  $\kappa = 0.11\phi^{5.6}d_S^2$  [83].

The Sauter diameter  $d_S$ , permeability  $\kappa$ , and Rayleigh number Ra for all sites investigated are provided in Table IV. Uncertainty ranges for Ra are calculated as systematic errors based on standard errors of all the input environmental parameters.

### APPENDIX D: EVAPORATION RATE

Groundwater evaporation rates are taken from the literature. At Owens Lake, Tyler *et al.* [37] combined lysimeter, Bowen ratio, and eddy correlation methods, with repeat seasonal measurements conducted well after any rainfall. The value of  $E = 0.4 \pm 0.1$  mm/day captures the range of measurements at their NFIP (North Flood Irrigation Project) site near our northern sites at the lake. At Badwater Basin, DeMeo *et al.* [38] measured

evaporation by Bowen ratio and eddy correlation methods, with continuous monitoring over several years. The value of  $E = 0.3 \pm 0.1$  mm/day is taken from their two playa sites south of Furnace Creek, and the 2001 conditions most consistent with the wetter season preceding our field work. At Sua Pan, we use  $E = 0.7 \pm 0.5$  mm/day estimated by remote sensing and energy balances [39], and wind tunnel experiments [35].

### APPENDIX E: TLS DATA PROCESSING

TLS scan data are processed following Ref. [22]. Data are first gridded into a digital elevation map (DEM) with a lateral resolution of 1 cm and a vertical resolution of 0.3 mm. Dominant frequencies of surface roughness, which we use here for the pattern wave number  $a$  (and wavelength  $\lambda = 2\pi/a$  as reported in Table IV) are then quantified using the 90th percentiles determined with the zero-upcrossing method from the DEMs [15]. TLS data from the U.S. field sites are deposited in Ref. [88]. The average pattern wave numbers from each of the three salt lakes visited are compared to their groundwater evaporation rates in Fig. 11.

### APPENDIX F: SALINITY AND DENSITY MEASUREMENTS

Owens Lake and Badwater Basin soil samples are analyzed to determine the amount of salt in their pore fluid. These samples are sealed immediately after collection to preserve their water content. After unsealing, each sample is first transferred to a crystallizing dish and weighed to give a combined mass of sand, salt, and water. It is then dried at 80 °C until all moisture visibly vanishes or for at least 24 h, and reweighed to determine the mass of the (evaporated) water. Next, it is washed with 50 ml of deionized water to dissolve any salt, allowed to sediment for 24 h, and the supernatant liquid is collected in another crystallizing dish. After two such washings, the remaining soil and the recovered salt solution are dried and weighed. Measurement uncertainty is based on the difference between the initial sample mass and the sum of the separated water ( $m_w$ ), salt ( $m_s$ ), and soil masses. This gives a direct measure of the mass fraction of salt in solution as  $C = m_s/(m_w + m_s)$  reported as a weight % (wt %).

Owens Lake pore water samples are analyzed to determine their density using a vibrating-tube densitometer (Anton Paar DMA4500). The near-surface (0–10 cm depth) groundwater density is consistently  $1255 \pm 8$  kg m<sup>-3</sup>, while water from 70–100 cm depth has a density of  $1050 \pm 2$  kg m<sup>-3</sup>. These values are broadly consistent with chloride concentration profiles previously measured at Owens Lake [37]. We note that thermal effects on the groundwater density are comparatively negligible, as the mean annual variation in temperature at Owens Lake allows for a density change of, at most, 5 kg m<sup>-3</sup>. Similarly, the

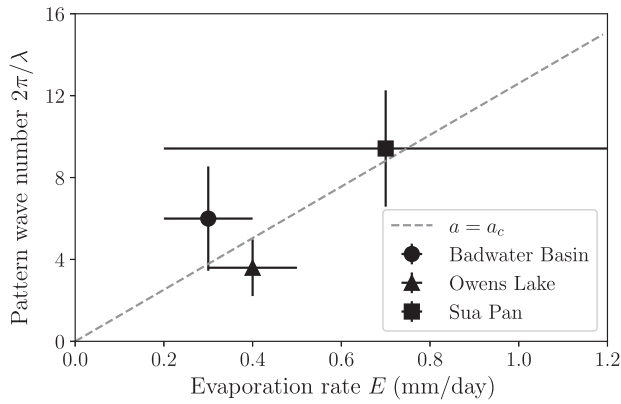


FIG. 11. The wave numbers of the surface crust patterns are compared to the local evaporation rates for field sites at Badwater Basin (dot), Owens Lake (triangle), and Sua Pan (square). Error bars in  $a$  show the standard deviation of measurements (see Table IV) at each site, while error bars in  $E$  reflect measurement uncertainties in evaporation rate [35,37–39]. For comparison with the model results, the dashed line shows the case where  $a = a_c$ .

solubility of halite in water will change by less than  $5 \text{ kg m}^{-3}$  seasonally. Data from salt concentration and pore water density measurements are deposited in Ref. [89].

### APPENDIX G: SALT CHEMISTRY AND DIFFUSIVITY

Pore water samples from selected sites at Owens Lake and Badwater Basin are analyzed to determine the dominant salt species present. This analysis is performed on the dried salts remaining after the salinity measurements (Appendix F). Mineral identification is performed by quantitative x-ray powder diffraction analysis (Philips X’Pert MPD PW 3040). Samples from Owens Lake show a mixture of salts with  $(53 \pm 7)$ -wt % sodium chloride and  $(30 \pm 5)$ -wt % hydrated sodium sulfate (mirabilite). Other minerals, such as natrite, sylvite, and burkeite, are variously

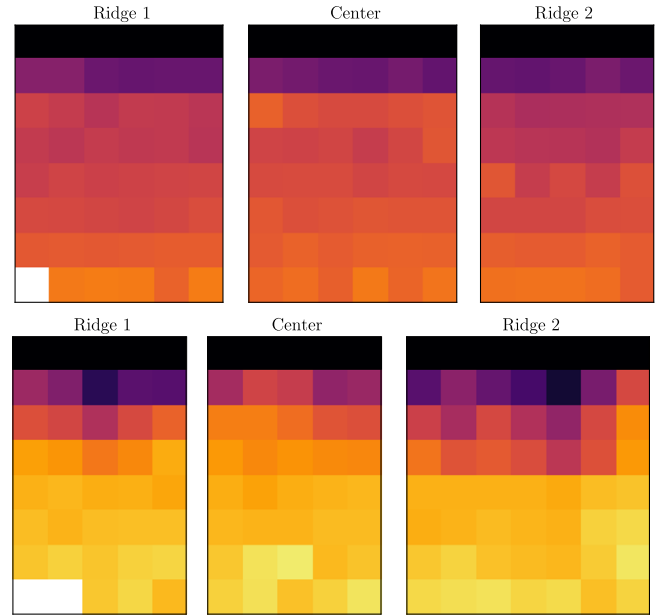


FIG. 12. Division of data from the two trench sites into two ridge areas and one center area each. The horizontal sample spacing is 15 cm. White areas indicate missing samples.

present at less than 10 wt %, each. As such, in solution  $\text{Na}^+$  and  $\text{Cl}^-$  ions predominate ( $>70\%$  by mass), with  $\text{SO}_4^{2-}$ ,  $\text{CO}_3^{2-}$ , and  $\text{K}^+$  ions present in descending order of significance. All data are deposited in Ref. [84].

Based on the ionic species found in the pore water, we estimate an average aqueous diffusivity of  $D^* = 1.37 \times 10^{-9} \text{ m}^2 \text{ s}^{-1}$  from measurements of ternary mixtures of the two primary salts [110] using a weighted average of the mole ratios of their main-term diffusion coefficients. Accounting for the tortuosity  $\theta$  of the porous medium, we then calculate an effective diffusion coefficient  $D = D^*/\theta^2 = (1.00 \pm 0.24) \times 10^{-9} \text{ m}^2 \text{ s}^{-1}$  following Ref. [75], where we estimate  $\theta^2 = 1 - \ln(\phi)$ , as in Ref. [74].

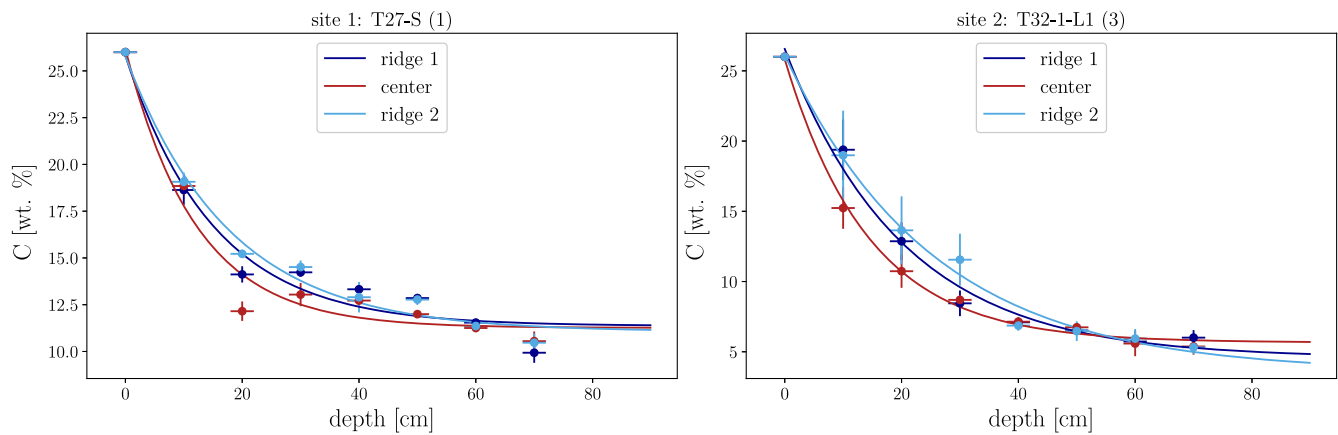


FIG. 13. Horizontally averaged salt concentration  $C(z)$ , at the ridge (blue) and center regions (red) of the two trench sites (dots) along with exponential fits (lines). Error bars indicate standard deviations of the concentrations, along with a sample position uncertainty of  $\pm 2 \text{ cm}$ .

TABLE II. Boundary-layer thickness  $L'$  along with the salt content (wt %) of background ( $C_{\text{bkg}}$ ) and saturated ( $C_{\text{sat}}$ ) pore fluid, from exponential fits to the salt concentration distributions below the center and ridge areas of two trench sites.

Site	Area	$L'$ (cm)	$C_{\text{bkg}}$ (wt %)	$C_{\text{sat}}$ (wt %)
Site 1	Ridge 1	$15.1 \pm 3.3$	$11.4 \pm 0.8$	$25.8 \pm 2.1$
Site 1	Ridge 2	$17.8 \pm 2.6$	$11.1 \pm 0.6$	$25.8 \pm 1.5$
Site 1	Center	$12.1 \pm 2.6$	$11.3 \pm 0.7$	$26.2 \pm 2.0$
Site 2	Ridge 1	$20.3 \pm 2.6$	$4.6 \pm 0.9$	$26.6 \pm 2.0$
Site 2	Ridge 2	$25.3 \pm 3.4$	$3.6 \pm 1.1$	$26.1 \pm 2.2$
Site 2	Center	$14.5 \pm 1.0$	$5.7 \pm 0.4$	$25.8 \pm 0.9$

### APPENDIX H: FITTING THE SALT-RICH BOUNDARY LAYER

We use the distributions of salt at the two trench sites to estimate the near-surface gradients in salt concentration, and from this the surface salt flux  $J_{c,z}$ . For this, we divide the grid of measurements at each site into ridge and center areas as shown in Fig. 12. Ridge areas cover about 40 cm on either side of a polygon ridge. The centers include samples from the areas between the ridges and are approximately 70 cm wide. An exponential of the form  $C(z) = C_{\text{bkg}} + (C_{\text{sat}} - C_{\text{bkg}})e^{z/L'}$  is then fit to the horizontally averaged salt concentrations ( $C$ , wt %) of each respective area, using an error-weighted fitting of the data. Here,  $L'$  is the effective thickness of the salt-rich boundary layer,  $C_{\text{bkg}}$  is a background salt content of the pore fluid at depth, and  $C_{\text{sat}}$  is the salt content of fluid at the surface. The fits are demonstrated in Fig. 13, and output values for the fit parameters are given in Table II, with associated errors. As a consistency check, we note that all fitted  $C_{\text{sat}}$  values agree with the mass fraction of a saturated NaCl solution (26.3 wt % at 10 °C [111]), which is by far the most predominant dissolved salt in the pore water at Owens Lake (see Appendix G). Following fitting, the salt concentrations, in terms of a weight per unit volume, are calculated as  $c = \rho C$ , assuming densities  $\rho$  based on NaCl solutions at 10 °C [112].

### APPENDIX I: EXPERIMENTAL METHODS

Experiments are performed in  $40 \times 20 \times 0.8$  cm (width  $\times$  height  $\times$  gap spacing) Hele-Shaw cells. As summarized in Table III, these are filled with glass beads (Sigmund Lindner GmbH) with diameters of 0–20 to 200–300  $\mu\text{m}$ ,  $d_s = 1.9 \pm 0.2$  to  $264 \pm 25$   $\mu\text{m}$ , and  $\varphi = 0.37 \times 10^{-2}$  to  $\varphi = 0.21 \times 10^{-2}$ . The permeability of the bead packs is evaluated by flow-through experiments. The base of each cell is connected to a reservoir containing a  $50\text{-kg m}^{-3}$  solution of NaCl, such that  $\Delta\rho = 162\text{ kg m}^{-3}$  (compared to a saturated salt solution [111]). This reservoir maintains a fluid-saturated pore space between the beads. Evaporation at the top of the cells is controlled and enhanced by overhead heating and air circulation and can be controlled from  $E \approx 1$  mm/day to 10 cm/day. Assuming a kinematic viscosity of  $\mu = 10^{-3}$  Pa s, these conditions allow for experiments from  $\text{Ra} = (7 \pm 2) \times 10^{-3}$  to  $\text{Ra} = (1.3 \pm 0.3) \times 10^3$ . The experiments with  $\text{Ra} < \text{Ra}_c$  do not show any convective dynamics over a period of three months, while all experiments with  $\text{Ra} > \text{Ra}_c$  show convection.

Visualization of the convective dynamics in the cells (see Supplemental Material Video S4 [72]) is accomplished by intermittently injecting 2–4 ml of dyed saline solution through a thin tube embedded in the cell. The dye is then advected by the flows inside the cell over time. Dye movement is recorded using time-lapse photography with a digital SLR camera (Nikon D5000 series). All experiments that report convection were already showing significant convective flows by the time of the first dye injection, at most 24 hours after they were set up, and there was no significant difference in these results, and subsequent dye injections.

To determine the experimental concentration profile shown in Fig. 6, one Hele-Shaw experiment at  $\text{Ra} = 120 \pm 13$  is destructively sampled. After two months of operation, the reservoir fluid is first dyed with rhodamine and then fluorescein to visualize the downwelling (dark, rhodamine) and upwelling (light, fluorescein) plumes. Once the dynamics of the plumes become

TABLE III. Details of experimental tests of the onset of convection including grain sizes (from manufacturer) of the glass beads used, along with the Sauter diameter  $d_s$ , permeability  $\kappa$ , porosity  $\varphi$ , evaporation rate  $E$ , and Rayleigh number  $\text{Ra}$ .

Grain size	$d_s$ ( $\mu\text{m}$ )	$\kappa$ ( $\text{m}^2$ )	$\varphi$	$E$ ( $\text{ms}^{-1}$ )	$\text{Ra}$	Convect
0–20	$1.9 \pm 0.2$	$(1.5 \pm 0.3) \times 10^{-15}$	0.37	$(3.6 \pm 1.0) \times 10^{-7}$	$0.007 \pm 0.002$	No
70–110	$86 \pm 9$	$(0.8 \pm 0.1) \times 10^{-11}$	0.32	$(6.1 \pm 2.4) \times 10^{-7}$	$20 \pm 9$	Yes
90–150	$123 \pm 12$	$(1.4 \pm 0.1) \times 10^{-11}$	0.30	$(3.6 \pm 1.0) \times 10^{-7}$	$64 \pm 19$	Yes
100–200	$150 \pm 15$	$(1.7 \pm 0.1) \times 10^{-11}$	0.28	$(3.6 \pm 1.0) \times 10^{-7}$	$74 \pm 22$	Yes
150–250	$214 \pm 20$	$(4.7 \pm 0.2) \times 10^{-11}$	0.24	$(3.6 \pm 1.0) \times 10^{-7}$	$207 \pm 59$	Yes
200–300	$264 \pm 25$	$(8.3 \pm 0.3) \times 10^{-11}$	0.21	$(1.0 \pm 0.3) \times 10^{-7}$	$1298 \pm 300$	Yes

TABLE IV. Sauter diameter  $d_S$ , permeability  $\kappa$ , Rayleigh number Ra, lower Ra limit  $Ra_L$ , upper Ra limit  $Ra_U$ , and pattern wavelength  $\lambda$  measured or calculated for each of the field sites at Badwater Basin, Owens Lake, and Sua Pan. For each site, longitude, latitude, and year of the field campaign are also given. Samples stemming from a trench are indicated as (\*).

Site	$d_S$ ( $\mu\text{m}$ )	$\kappa \times 10^{-11}$ ( $\text{m}^2$ )	Ra ( $Ra_L$ ; $Ra_U$ )	$\lambda$ (m)	Latitude	Longitude	Year
Death Valley							
Badwater Basin (1)	$59 \pm 15$	$4.99 \pm 2.95$	28 643 (8374; 93 961)	$1.42 \pm 0.58$	$36^\circ 13.651'$	$-116^\circ 46.723'$	2016
Badwater Basin (2)	$66 \pm 12$	$6.24 \pm 2.91$	35 793 (12 736; 103 415)	$1.42 \pm 0.58$	$36^\circ 13.674'$	$-116^\circ 46.735'$	2016
Badwater Basin (3)	$67 \pm 9$	$6.52 \pm 2.56$	37 444 (15 096; 98 635)	$1.27 \pm 0.55$	$36^\circ 13.665'$	$-116^\circ 46.820'$	2016
Badwater Basin (4)	$72 \pm 3$	$7.39 \pm 2.29$	42 419 (20 975; 93 764)	$0.58 \pm 0.32$	$36^\circ 13.660'$	$-116^\circ 46.903'$	2016
Badwater Basin (5)	$50 \pm 15$	$3.10 \pm 2.35$	21 064 (5692; 72 316)	$0.55 \pm 0.28$	$36^\circ 13.654'$	$-116^\circ 47.036'$	2016
Owens Lake							
T10-3	$4.3 \pm 0.6$	$0.03 \pm 0.02$	117 (48; 286)	$1.79 \pm 0.86$	$36^\circ 23.147'$	$-117^\circ 56.772'$	2018
T16	$6.8 \pm 1.6$	$0.07 \pm 0.04$	294 (99; 828)	$1.19 \pm 0.51$	$36^\circ 23.953'$	$-117^\circ 56.454'$	2018
T2-4	$29 \pm 14$	$1.23 \pm 1.12$	5457 (918; 21 627)	$1.13 \pm 0.54$	$36^\circ 20.803'$	$-117^\circ 58.642'$	2016
T2-5 (1)	$24 \pm 4$	$0.81 \pm 0.35$	3594 (1443; 8953)	$1.04 \pm 0.41$	$36^\circ 21.055'$	$-117^\circ 58.824'$	2016
T2-5 (2)	$20 \pm 3$	$0.55 \pm 0.22$	2436 (1052; 5742)	$0.94 \pm 0.50$	$36^\circ 20.895'$	$-117^\circ 58.740'$	2016
T2-5 (3)	$18 \pm 3$	$0.46 \pm 0.18$	2033 (886; 4762)	$1.62 \pm 0.65$	$36^\circ 20.877'$	$-117^\circ 58.711'$	2018
T25-3 (1)	$11 \pm 2$	$0.17 \pm 0.08$	771 (300; 1967)	$2.25 \pm 0.89$	$36^\circ 27.039'$	$-117^\circ 54.510'$	2018
T25-3 (2)	$24 \pm 4$	$0.83 \pm 0.36$	3697 (1484; 9211)	$1.18 \pm 0.56$	$36^\circ 28.383'$	$-117^\circ 54.957'$	2018
T27-A (1)	$31 \pm 8$	$1.35 \pm 0.81$	5994 (1843; 17825)	$1.70 \pm 0.65$	$36^\circ 29.302'$	$-117^\circ 55.953'$	2016
T27-A (2)	$33 \pm 4$	$1.55 \pm 0.56$	6916 (3149; 15 614)	$2.72 \pm 0.98$	$36^\circ 29.061'$	$-117^\circ 55.602'$	2016
T27-A (3)	$22 \pm 3$	$0.71 \pm 0.26$	3172 (1453; 7126)	$1.44 \pm 0.55$	$36^\circ 29.112'$	$-117^\circ 55.804'$	2018
T27S (*)	$21 \pm 6$	$0.65 \pm 0.42$	2892 (836; 8913)	$1.51 \pm 0.64$	$36^\circ 28.549'$	$-117^\circ 54.994'$	2018
T29-3 (1)	$138 \pm 23$	$27.42 \pm 12.20$	121 991 (47 476; 310 939)	$3.02 \pm 1.40$	$36^\circ 29.955'$	$-117^\circ 55.999'$	2016
T29-3 (2)	$116 \pm 22$	$19.49 \pm 9.29$	86 704 (32 068; 229 077)	$2.80 \pm 1.34$	$36^\circ 29.960'$	$-117^\circ 55.962'$	2016
T32-1-L1 (1) (*)	$36 \pm 12$	$1.84 \pm 1.35$	8188 (2018; 27 469)	$1.56 \pm 0.66$	$36^\circ 53.897'$	$-117^\circ 57.209'$	2016
T32-1-L1 (2) (*)	$20 \pm 4$	$0.56 \pm 0.26$	2492 (946; 6467)	$2.65 \pm 0.98$	$36^\circ 32.354'$	$-117^\circ 57.218'$	2018
T32-1-L1 (3) (*)	$37 \pm 10$	$2.01 \pm 1.18$	8923 (2784; 26 303)	$2.43 \pm 0.92$	$36^\circ 32.337'$	$-117^\circ 57.204'$	2018
T36-3 (1)	$46 \pm 4$	$3.04 \pm 1.01$	13 538 (6483; 29 282)	$1.17 \pm 0.91$	$36^\circ 29.953'$	$-117^\circ 58.505'$	2016
T36-3 (2)	$35 \pm 8$	$1.82 \pm 0.99$	8086 (2689; 22 918)	$2.27 \pm 1.03$	$36^\circ 30.050'$	$-117^\circ 58.518'$	2016
T36-3 (3)	$75 \pm 25$	$8.08 \pm 5.83$	35924 (9027; 119336)	$1.43 \pm 0.62$	$36^\circ 29.724'$	$-117^\circ 57.916'$	2016
T8-W	$8.7 \pm 2.6$	$0.11 \pm 0.08$	485 (135; 1527)	$0.87 \pm 0.41$	$36^\circ 22.522'$	$-117^\circ 57.256'$	2018
Sua Pan							
B7	$9.6 \pm 0.9$	$0.13 \pm 0.05$	341 (117; 1683)	$0.92 \pm 0.48$	$-20^\circ 35.046'$	$25^\circ 54.654'$	2012
L5	$11.6 \pm 1.1$	$0.20 \pm 0.08$	497 (170; 2456)	$0.59 \pm 0.22$	$-20^\circ 33.996'$	$26^\circ 0.420'$	2012
D10	$10.6 \pm 1.4$	$0.16 \pm 0.07$	415 (131; 2198)	$0.41 \pm 0.16$	$-20^\circ 36.678'$	$25^\circ 55.794'$	2012
J11	$10.6 \pm 1.4$	$0.16 \pm 0.07$	415 (131; 2198)	$0.69 \pm 0.27$	$-20^\circ 37.242'$	$25^\circ 59.250'$	2012
B3	$10.6 \pm 1.4$	$0.16 \pm 0.07$	415 (131; 2198)	$0.58 \pm 0.22$	$-20^\circ 32.880'$	$25^\circ 54.672'$	2012
D5	$10.6 \pm 1.4$	$0.16 \pm 0.07$	415 (131; 2198)	$0.95 \pm 0.33$	$-20^\circ 33.972'$	$25^\circ 55.818'$	2012
I4	$10.6 \pm 1.4$	$0.16 \pm 0.07$	415 (131; 2198)	$0.53 \pm 0.20$	$-20^\circ 33.447'$	$25^\circ 58.699'$	2012

apparent, the wet bead packing in the cell is removed in layers, while sampling every 2 cm in depth along the centers of the plumes. The resulting approximately 1-ml samples are analyzed for their salt concentration using the same protocol as described for the field samples in Appendix F.

[1] NPS Stats: National Park Service Visitor Use Statistics, <https://irma.nps.gov/Stats/Reports/Park/DEVA> (accessed on January 30, 2022).

[2] T.K. Lowenstein and L.A. Hardie, *Criteria for the Recognition of Salt-Pan Evaporites*, *Sedimentology* **32**, 627 (1985).

[3] T.E. Gill, *Eolian Sediments Generated by Anthropogenic Disturbance of Playas: Human Impacts on the Geomorphic System and Geomorphic Impacts on the Human System*, *Geomorphology* **17**, 207 (1996).

[4] P.R. Briere, *Playa, Playa Lake, Sabkha: Proposed Definitions for Old Terms*, *J. Arid Environ.* **45**, 1 (2000).

[5] R. Bryant and M. Rainey, *Investigation of Flood Inundation on Playas within the Zone of Chotts, Using a Time-Series of AVHRR*, *Remote Sens. Environ.* **82**, 360 (2002).

[6] J.M. Prospero, *Environmental Characterization of Global Sources of Atmospheric Soil Dust Identified with the NIMBUS 7 Total Ozone Mapping Spectrometer (TOMS) Absorbing Aerosol Product*, *Rev. Geophys.* **40**, 2-1-2-31 (2002).

[7] M. Klose, T.E. Gill, Vicken Etyemezian, G. Nikolich, Z. G. Zadeh, N. P. Webb, and R. S. V. Pelt, *Dust Emission*

- from Crusted Surfaces: Insights from Field Measurements and Modelling, *Aeolian Res.* **40**, 1 (2019).
- [8] X. Li and F. Shi, *Effects of Evolving Salt Precipitation on the Evaporation and Temperature of Sandy Soil with a Fixed Groundwater Table*, *Vadose Zone J.* **20**, e20122 (2021).
- [9] G. E. Ericksen, J. D. Vine, and R. Ballon, *Chemical Composition and Distribution of Lithium-Rich Brines in Salar de Uyuni and Nearby Salars in Southwestern Bolivia*, in *Lithium Needs and Resources* (Elsevier, New York, 1978), pp. 355–363, [10.1016/B978-0-08-022733-7.50020-4](https://doi.org/10.1016/B978-0-08-022733-7.50020-4).
- [10] G. Wadge, D. Archer, and A. Millington, *Monitoring Playa Sedimentation Using Sequential Radar Images*, *Terra Nova* **6**, 391 (1994).
- [11] J. Lasser, J. M. Nield, and L. Goehring, *Surface and Subsurface Characterisation of Salt Pans Expressing Polygonal Patterns*, *Earth Syst. Sci. Data* **12**, 2881 (2020).
- [12] D. Krinsley, *A Geomorphological and Paleoclimatological Study of the Playas of Iran. Part 1*, U.S. Geological Survey Report No. CP 70-800 (U.S. GPO, Washington, DC, 1970).
- [13] Y. Dang, L. Xiao, Y. Xu, F. Zhang, J. Huang, J. Wang, J. Zhao, G. Komatsu, and Z. Yue, *The Polygonal Surface Structures in the Dalangtan Playa, Qaidam Basin, NW China: Controlling Factors for Their Formation and Implications for Analogous Martian Landforms*, *J. Geophys. Res. Planets* **123**, 1910 (2018).
- [14] W. E. Sanford and W. W. Wood, *Hydrology of the Coastal Sabkhas of Abu Dhabi, United Arab Emirates*, *Hydrogeol. J.* **9**, 358 (2001).
- [15] J. M. Nield, R. G. Bryant, G. F. Wiggs, J. King, D. S. Thomas, F. D. Eckardt, and R. Washington, *The Dynamism of Salt Crust Patterns on Playas*, *Geology* **43**, 31 (2015).
- [16] V. R. Martínez, C. I. Galli, and R. N. Alonso, *Morfología de las costras evaporíticas del salar de Pozuelos, Puna Salteña*, *Rev. Asoc. Geol. Argent.* **77**, 163 (2020), <https://ri.conicet.gov.ar/handle/11336/142607>.
- [17] F. W. Christiansen, *Polygonal Fracture and Fold Systems in the Salt Crust, Great Salt Lake Desert, Utah*, *Science* **139**, 607 (1963).
- [18] S. Lokier, *Development and Evolution of Subaerial Halite Crust Morphologies in a Coastal Sabkha Setting*, *J. Arid Environ.* **79**, 32 (2012).
- [19] J. C. Dixon, *Aridic Soils, Patterned Ground, and Desert Pavements*, in *Geomorphology of Desert Environments* (Springer, Dordrecht, 2009), pp. 101–122, [10.1007/978-1-4020-5719-9\\_5](https://doi.org/10.1007/978-1-4020-5719-9_5).
- [20] P. D. Deckker, *Biological and Sedimentary Facies of Australian Salt Lakes*, *Palaeogeography, palaeoclimatology, palaeoecology* **62**, 237 (1988).
- [21] F. D. Eckardt, R. G. Bryant, G. McCulloch, B. Spiro, and W. W. Wood, *The Hydrochemistry of a Semi-Arid Pan Basin Case Study: Sua Pan, Makgadikgadi, Botswana*, *Applied geochemistry : Journal of the International Association of Geochemistry and Cosmochemistry* **23**, 1563 (2008).
- [22] J. M. Nield, J. King, G. F. S. Wiggs, J. Leyland, R. G. Bryant, R. C. Chiverrell, S. E. Darby, F. D. Eckardt, D. S. G. Thomas, L. H. Vircavs, and R. Washington, *Estimating Aerodynamic Roughness over Complex Surface Terrain*, *J. Geophys. Res. Atmos.* **118**, 12,948 (2013).
- [23] R. Milewski, S. Chabrillat, and B. Bookhagen, *Analyses of Namibian Seasonal Salt Pan Crust Dynamics and Climatic Drivers Using Landsat 8 Time-Series and Ground Data*, *Remote Sens.* **12**, 474 (2020).
- [24] R. L. Reynolds, J. C. Yount, M. Reheis, H. Goldstein, J. Pat Chavez, R. Fulton, J. Whitney, C. Fuller, and R. M. Forester, *Dust Emission from Wet and Dry Playas in the Mojave Desert, USA*, *Earth Surf. Processes Landforms* **32**, 1811 (2007).
- [25] I. Y. Fung, S. K. Meyn, I. Tegen, S. C. Doney, J. G. John, and J. K. B. Bishop, *Iron Supply and Demand in the Upper Ocean*, *Global Biogeochem Cycles* **14**, 281 (2000).
- [26] T. A. Cahill, T. E. Gill, J. S. Reid, E. A. Gearhart, and D. A. Gillette, *Saltating Particles, Playa Crusts and Dust Aerosols at Owens (Dry) Lake, California*, *Earth Surf. Processes Landforms* **21**, 621 (1996).
- [27] T. E. Gill, D. A. Gillette, T. Niemeier, and R. T. Winn, *Elemental Geochemistry of Wind-Erodible Playa Sediments, Owens Lake, California*, *Nucl. Instrum. Methods Phys. Res., Sect. B* **189**, 209 (2002).
- [28] *National Academies of Sciences, Engineering, and Medicine, Effectiveness and Impacts of Dust Control Measures for Owens Lake* (The National Academies Press, Washington, DC, 2020), [10.17226/25658](https://doi.org/10.17226/25658).
- [29] D. P. Groeneveld, J. L. Huntington, and D. D. Barz, *Floating Brine Crusts, Reduction of Evaporation and Possible Replacement of Fresh Water to Control Dust from Owens Lake Bed, California*, *J. Hydrol.* **392**, 211 (2010).
- [30] D. P. Groeneveld and D. D. Barz, *Remote Monitoring of Surfaces Wetted for Dust Control on the Dry Owens Lakebed, California*, *Open J. Mod. Hydro.* **03**, 241 (2013).
- [31] Heather J. Tollerud and Matthew S. Fantle, *The Temporal Variability of Centimeter-Scale Surface Roughness in a Playa Dust Source: Synthetic Aperture Radar Investigation of Playa Surface Dynamics*, *Remote Sens. Environ.* **154**, 285 (2014).
- [32] M. C. Baddock, P. Ginoux, J. E. Bullard, and T. E. Gill, *Do MODIS-Defined Dust Sources Have a Geomorphological Signature?*, *Geophys. Res. Lett.* **43**, 2606 (2016).
- [33] M. R. Sweeney, V. A. Zlotnik, R. M. Joeckel, and J. E. Stout, *Geomorphologic and Hydrologic Controls of Dust Emissions during Drought from Yellow Lake Playa, West Texas, USA*, *J. Arid Environ.* **133**, 37 (2016).
- [34] R. G. Bryant, *Recent Advances in Our Understanding of Dust Source Emission Processes*, *Prog. Phys. Geol.* **37**, 397 (2013).
- [35] J. M. Nield, C. M. Neuman, P. O'Brien, R. G. Bryant, and G. F. Wiggs, *Evaporative Sodium Salt Crust Development and Its Wind Tunnel Derived Transport Dynamics under Variable Climatic Conditions*, *Aeolian Res.* **23**, 51 (2016).
- [36] H. Eloukabi, N. Sghaier, S. B. Nasrallah, and M. Prat, *Experimental Study of the Effect of Sodium Chloride on Drying of Porous Media: The Crusty-Patchy Efflorescence Transition*, *Int. J. Heat Mass Transfer* **56**, 80 (2013).
- [37] S. Tyler, S. Kranz, M. Parlange, J. Albertson, G. Katul, G. Cochran, B. Lyles, and G. Holder, *Estimation of Groundwater Evaporation and Salt Flux from Owens Lake, California, USA*, *J. Hydrol.* **200**, 110 (1997).

- [38] G. A. DeMeo, R. J. Lacznia, R. A. Boyd, J. L. Smith, and W. E. Nylund, *Estimated Ground-Water Discharge by Evapotranspiration from Death Valley, California, 1997–2001*, U.S. Geological Survey Report No. 03-4254, [10.3133/wri034254](https://doi.org/10.3133/wri034254) (2003).
- [39] P. Brunner, P. Bauer, M. Eugster, and W. Kinzelbach, *Using Remote Sensing to Regionalize Local Precipitation Recharge Rates Obtained from the Chloride Method*, *J. Hydrol.* **294**, 241 (2004).
- [40] S. K. Kampf, S. W. Tyler, C. A. Ortiz, J. F. Munoz, and P. L. Adkins, *Evaporation and Land Surface Energy Budget at the Salar de Atacama, Northern Chile*, *J. Hydrol.* **310**, 236 (2005).
- [41] W. W. Wood, W. E. Sanford, and A. R. S. A. Habshi, *Source of Solutes to the Coastal Sabkha of Abu Dhabi*, *JSA Bull.* **114**, 259 (2002).
- [42] R. Wooding, *Rayleigh Instability of a Thermal Boundary Layer in Flow through a Porous Medium*, *J. Fluid Mech.* **9**, 183 (1960).
- [43] G. M. Homsy and A. E. Sherwood, *Convective Instabilities in Porous Media with Through Flow*, *AIChE J.* **22**, 168 (1976).
- [44] R. A. Wooding, S. W. Tyler, I. White, and P. A. Anderson, *Convection in Groundwater below an Evaporating Salt Lake: 2. Evolution of Fingers or Plumes*, *Water Resour. Res.* **33**, 1219 (1997).
- [45] R. A. Wooding, *Variable-Density Saturated Flow with Modified Darcy's Law: The Salt Lake Problem and Circulation*, *Water Resour. Res.* **43** (2007).
- [46] R. L. Van Dam, C. T. Simmons, D. W. Hyndman, and W. W. Wood, *Natural Free Convection in Porous Media: First Field Documentation in Groundwater*, *Geophys. Res. Lett.* **36**, L11403 (2009).
- [47] L. Goehring, L. Mahadevan, and S. W. Morris, *Nonequilibrium Scale Selection Mechanism for Columnar Jointing*, *Proc. Natl. Acad. Sci. U.S.A.* **106**, 387 (2009).
- [48] A. H. Lachenbruch, *Mechanics of Thermal Contraction Cracks and Ice-Wedge Polygons in Permafrost*, *U.S. Geol. Surv. Special Pap.* **70**, 69 (1962).
- [49] R. S. Sletten, B. Hallet, and R. C. Fletcher, *Resurfacing Time of Terrestrial Surfaces by the Formation and Maturation of Polygonal Patterned Ground*, *J. Geophys. Res.* **108**, 8044 (2003).
- [50] M. A. Kessler and B. T. Werner, *Self-Organization of Sorted Patterned Ground*, *Science* **299**, 380 (2003).
- [51] L. Goehring, *Evolving Fracture Patterns: Columnar Joints, Mud Cracks and Polygonal Terrain*, *Phil. Trans. R. Soc. A* **371**, 20120353 (2013).
- [52] X. Fu, L. Cueto-Felgueroso, and R. Juanes, *Pattern Formation and Coarsening Dynamics in Three-Dimensional Convective Mixing in Porous Media*, *Phil. Trans. R. Soc. A* **371**, 20120355 (2013).
- [53] Marco De Paoli, Sergio Pirozzoli, Francesco Zonta, and Alfredo Soldati, *Strong Rayleigh–Darcy Convection Regime in Three-Dimensional Porous Media*, *J. Fluid Mech.* **943**, A51 (2022).
- [54] S. G. Fryberger, A. M. Al-Sari, and T. J. Clisham, *Eolian Dune, Interdune, Sand Sheet, and Siliciclastic Sabkha Sediments of an Offshore Prograding Sand Sea, Dhahran Area, Saudi Arabia*, *AAPG bulletin* **67**, 280 (1983).
- [55] N. Bowden, S. Brittain, A. G. Evans, J. W. Hutchinson, and G. M. Whitesides, *Spontaneous Formation of Ordered Structures in Thin Films of Metals Supported on an Elastomeric Polymer*, *Nature (London)* **393**, 146 (1998).
- [56] L. Mahadevan and S. Rica, *Self-Organized Origami*, *Science* **307**, 1740 (2005).
- [57] B. Li, Y.-P. Cao, X.-Q. Feng, and H. Gao, *Mechanics of Morphological Instabilities and Surface Wrinkling in Soft Materials: A Review*, *Soft Matter* **8**, 5728 (2012).
- [58] J. Dervaux and M. B. Amar, *Mechanical Instabilities of Gels*, *Annu. Rev. Condens. Matter Phys.* **3**, 311 (2012).
- [59] A. H. Lachenbruch, *Depth and Spacing of Tension Cracks*, *J. Geophys. Res.* **66**, 4273 (1961).
- [60] K. A. Shorlin, J. R. de Bruyn, M. Graham, and S. W. Morris, *Development and Geometry of Isotropic and Directional Shrinkage-Crack Patterns*, *Phys. Rev. E* **61**, 6950 (2000).
- [61] R. M. Tucker, *Giant Polygons in the Triassic Salt of Cheshire, England; A Thermal Contraction Model for Their Origin*, *J. Sediment. Res.* **51**, 779 (1981).
- [62] M. T. Mellon, C. P. McKay, and J. L. Heldmann, *Polygonal Ground in the McMurdo Dry Valley of Antarctica and Its Relationship to Ice-Table Depth and the Recent Antarctic Climate History*, *Antarctic science / Blackwell Scientific Publications* **26**, 413 (2014).
- [63] M. Steiger and S. Asmussen, *Crystallization of Sodium Sulfate Phases in Porous Materials: The Phase Diagram Na<sub>2</sub>SO<sub>4</sub> – H<sub>2</sub>O and the Generation of Stress*, *Geochim. Cosmochim. Acta* **72**, 4291 (2008).
- [64] J. Lasser, M. Ernst, and L. Goehring, *Stability of Convection in Dry Salt Lakes*, *J. Fluid Mech.* **917**, A14 (2021).
- [65] J. D. Stevens, J. M. S., Jr., C. T. Simmons, and T. Fenstemaker, *Evidence of Free Convection in Groundwater: Field-Based Measurements beneath Wind-Tidal Flats*, *J. Hydrol.* **375**, 394 (2009).
- [66] J. A. Neufeld, M. A. Hesse, A. Riaz, M. A. Hallworth, H. A. Tchelepi, and H. E. Huppert, *Convective Dissolution of Carbon Dioxide in Saline Aquifers*, *Geophys. Res. Lett.* **37**, L22404 (2010).
- [67] A. C. Slim, *Solutal-Convection Regimes in a Two-Dimensional Porous Medium*, *J. Fluid Mech.* **741**, 461 (2014).
- [68] D. R. Hewitt, J. A. Neufeld, and J. R. Lister, *High Rayleigh Number Convection in a Porous Medium Containing a Thin Low-Permeability Layer*, *J. Fluid Mech.* **756**, 844 (2014).
- [69] C. Gueller and G. D. Thyne, *Hydrologic and Geologic Factors Controlling Surface and Groundwater Chemistry in Indian Wells–Owens Valley Area, Southeastern California, USA*, *J. Hydrol.* **285**, 177 (2004).
- [70] J. Ryu, R. A. Zierenberg, R. A. Dahlgren, and S. Gao, *Sulfur Biogeochemistry and Isotopic Fractionation in Shallow Groundwater and Sediments of Owens Dry Lake, California*, *Chem. Geol.* **229**, 257 (2006).

- [71] L. Nicholas and B. Andy, *Influence of Vegetation Cover on Sand Transport by Wind: Field Studies at Owens Lake, California*, *Earth Surf. Processes Landforms* **23**, 69 (1997).
- [72] See Supplemental Material at <http://link.aps.org/supplemental/10.1103/PhysRevX.13.011025> for four movies: one movie of growing salt patterns in the field, two movies of the fluid dynamics in two- and three dimensions, respectively, and one video of the fluid dynamics in a laboratory experiment.
- [73] C. van Duijn, G. Pieters, R. Wooding, and A. van der Ploeg, *Stability Criteria for the Vertical Boundary Layer Formed by Throughflow near the Surface of a Porous Medium*, in *Environmental Mechanics: Water, Mass and Energy Transfer in the Biosphere*, edited by P. A. Raats, D. Smiles, and A. W. Warrick (American Geophysical Union, Washington, DC, 2002), pp. 155–169, <https://research.tue.nl/en/publications/stability-criteria-for-the-boundary-layer-formed-by-throughflow-a-2>.
- [74] B. P. Boudreau, *The Diffusive Tortuosity of Fine-Grained Unlithified Sediments*, *Geochim. Cosmochim. Acta* **60**, 3139 (1996).
- [75] B. P. Boudreau, *Diagenetic Models and Their Implementation: Modelling Transport and Reactions in Aquatic Sediments* (Springer, New York, 2011).
- [76] M. Boufadel, M. Suidan, and A. Venosa, *Numerical Modeling of Water Flow below Dry Salt Lakes: Effect of Capillarity and Viscosity*, *J. Hydrol.* **221**, 55 (1999).
- [77] V. Loodts, L. Rongy, and A. De Wit, *Impact of Pressure, Salt Concentration, and Temperature on the Convective Dissolution of Carbon Dioxide in Aqueous Solutions*, *Chaos* **24**, 043120 (2014).
- [78] J. Elder, *Steady Free Convection in a Porous Medium Heated from Below*, *J. Fluid Mech.* **27**, 29 (1967).
- [79] D. Hewitt, *Vigorous Convection in Porous Media*, *Proc. R. Soc. A* **476**, 20200111 (2020).
- [80] D. R. Hewitt, J. A. Neufeld, and J. R. Lister, *Ultimate Regime of High Rayleigh Number Convection in a Porous Medium*, *Phys. Rev. Lett.* **108**, 224503 (2012).
- [81] J. Lasser and L. Goehring, *Grain Size Distributions of Sand Samples from Owens Lake and Badwater Basin in Central California, Collected in 2016 and 2018* (2020), [10.1594/PANGAEA.910996](https://doi.org/10.1594/PANGAEA.910996).
- [82] J. Sauter, *Die Grössenbestimmung der in Gemischnebeln von Verbrennungskraftmaschinen vorhandenen Brennstoffteilchen*, *VDI-Forschungsheft* **279** (1928), <https://www.worldcat.org/de/title/groenbestimmung-der-im-gemischnebel-von-verbrennungskraftmaschinen-vorhandenen-brennstoffteilchen/oclc/257620968>.
- [83] X. Garcia, L. T. Akanji, M. J. Blunt, S. K. Matthai, and J. P. Latham, *Numerical Study of the Effects of Particle Shape and Polydispersity on Permeability*, *Phys. Rev. E* **80**, 021304 (2009).
- [84] J. Lasser and V. Karius, *Chemical Characterization of Salt Samples from Owens Lake and Badwater Basin, Central California, Collected in 2016 and 2018* (2020), [10.1594/PANGAEA.911239](https://doi.org/10.1594/PANGAEA.911239).
- [85] R. A. Wooding, S. W. Tyler, I. White, and P. A. Anderson, *Convection in Groundwater below an Evaporating Salt Lake: I. Onset of Instability*, *Water Resour. Res.* **33**, 1199 (1997).
- [86] A. C. Slim, M. M. Bandi, J. C. Miller, and L. Mahadevan, *Dissolution-Driven Convection in a Hele-Shaw Cell*, *Phys. Fluids* **25**, 024101 (2013).
- [87] C. Thomas, S. Dehaeck, and A. D. Wit, *Convective Dissolution of CO<sub>2</sub> in Water and Salt Solutions*, *Int. J. Greenhouse Gas Contr.* **72**, 105 (2018).
- [88] J. M. Nield, J. Lasser, and L. Goehring, *TLS Surface Scans from Owens Lake and Badwater Basin, Central California, Measured in 2016 and 2018* (2020), [10.1594/PANGAEA.911054](https://doi.org/10.1594/PANGAEA.911054).
- [89] J. Lasser and L. Goehring, *Subsurface Salt Concentration Profiles and Pore Water Density Measurements from Owens Lake, Central California, Measured in 2018* (2020), [10.1594/PANGAEA.911233](https://doi.org/10.1594/PANGAEA.911233).
- [90] Uri Nachshon, Noam Weisbrod, Roei Katzir, and Ahmed Nasser, *NaCl Crust Architecture and Its Impact on Evaporation: Three-Dimensional Insights*, *Geophys. Res. Lett.* **45**, 6100 (2018).
- [91] N. Otsu, *A Threshold Selection Method from Gray-Level Histograms*, *IEEE Trans. Syst. Man Cybern.* **9**, 62 (1979).
- [92] Sheng Dai, Hosung Shin, and J. Carlos Santamarina, *Formation and Development of Salt Crusts on Soil Surfaces*, *Acta Geotech.* **11**, 1103 (2016).
- [93] G. Licsandru, C. Noiriel, P. Duru, S. Geoffroy, A. Abou Chakra, and M. Prat, *Dissolution-Precipitation-Driven Upward Migration of a Salt Crust*, *Phys. Rev. E* **100**, 032802 (2019).
- [94] Alexandra Mailleur, Christophe Pirat, Olivier Pierre-Louis, and Jean Colombani, *Hollow Rims from Water Drop Evaporation on Salt Substrates*, *Phys. Rev. Lett.* **121**, 214501 (2018).
- [95] A. Mojtabi and M.-C. Charrier-Mojtabi, *Double-Diffusive Convection in Porous Media*, in *Handbook of Porous Media*, edited by K. Vafai (CRC Press, Boca Raton, 2005), pp. 269–320, [10.1201/9780415876384](https://doi.org/10.1201/9780415876384).
- [96] IPCC, *Climate Change 2021: The Physical Science Basis*, V. Masson-Delmotte, P. Zhai, A. Pirani, S. L. Connors, C. Péan, S. Berger, N. Caud, Y. Chen, L. Goldfarb, M. I. Gomis, M. Huang, K. Leitzell, E. Lonnoy, J. B. R. Matthews, T. K. Maycock, T. Waterfield, O. Yelekçi, R. Yu, and B. Zhou (Cambridge University Press, Cambridge, England, 2021), Chap. 6, [10.1017/9781009157896](https://doi.org/10.1017/9781009157896).
- [97] E. Rodriguez-Caballero, T. Stanelle, S. Egerer, Y. Cheng, H. Su, Y. Canton, J. Belnap, M. O. Andreae, I. Tegen, C. H. Reick, U. Pöschl, and B. Weber, *Global Cycling and Climate Effects of Aeolian Dust Controlled by Biological Soil Crusts*, *Nat. Geosci.* **15**, 458 (2022).
- [98] W. A. Wurtsbaugh, C. Miller, S. E. Null, R. J. DeRose, P. Wilcock, M. Hahnenberger, F. Howe, and J. Moore, *Decline of the World's Saline Lakes*, *Nat. Geosci.* **10**, 816 (2017).
- [99] N. Juergens, *The Biological Underpinnings of Namib Desert Fairy Circles*, *Science* **339**, 1618 (2013).
- [100] J. Lasser, L. Goehring, and J. M. Nield, *Images and Videos from Owens Lake and Badwater Basin in Central California, Taken in 2016 and 2018* (2020), [10.1594/PANGAEA.911054](https://doi.org/10.1594/PANGAEA.911054).
- [101] Jana Lasser (2022), [10.5281/zenodo.3969492](https://doi.org/10.5281/zenodo.3969492).

- [102] Jana Lasser, *Salt Polygons and Porous Media Convection* (2022), [10.17605/OSF.IO/KJDWF](https://doi.org/10.17605/OSF.IO/KJDWF).
- [103] C. Canuto, M. Y. Hussaini, A. Quarteroni, and T. A. Z., Jr., *Spectral Methods in Fluid Dynamics* (Springer, New York, 1988), [10.1007/978-3-642-84108-8](https://doi.org/10.1007/978-3-642-84108-8).
- [104] G. E. Karniadakis, M. Israeli, and S. A. Orszag, *High-Order Splitting Methods for the Incompressible Navier-Stokes Equations*, *J. Comput. Phys.* **97**, 414 (1991).
- [105] A. Riaz and E. Meiburg, *Three-Dimensional Miscible Displacement Simulations in Homogeneous Porous Media with Gravity Override*, *J. Fluid Mech.* **494**, 95 (2003).
- [106] C.-Y. Chen, *Topics in Miscible Porous Media Flows* (University of Southern California, Los Angeles, 1998).
- [107] K. J. Hollet, W. R. Danskin, W. F. McCaffrey, and C. L. Waiti, *Geology and Water Resources of Owens Valley California* (U.S. GPO, Washington, DC, 1991), [10.3133/ofr88715](https://doi.org/10.3133/ofr88715).
- [108] C. B. Hunt, T. Robinson, W. Bowles, and A. Washburn, *Hydrologic Basin, Death Valley, California*, U.S. Geol. Surv. Prof. Paper (1966), [10.3133/pp494B](https://doi.org/10.3133/pp494B).
- [109] *Los Angeles Department of Water and Power, Owens Lake Habitat Management Plan* (2010), <https://www.inyowater.org/wp-content/uploads/2013/11/Owens-Valley-Land-Management-Plan-Final.pdf>.
- [110] O. Annunziata, J. A. Rard, J. G. Albright, L. Paduano, and D. G. Miller, *Mutual Diffusion Coefficients and Densities at 298.15 K of Aqueous Mixtures of NaCl and Na<sub>2</sub>SO<sub>4</sub> for Six Different Solute Fractions at a Total Molarity of 1.500 mol · dm<sup>3</sup> and of Aqueous Na<sub>2</sub>SO<sub>4</sub>*, *J. Chem. Eng. Data* **45**, 936 (2000).
- [111] *Solubility Data Series*, edited by R. Cohen-Adad and J. W. Lorimer (Pergamon, New York, 1991), Vol. 47.
- [112] *Perry's Chemical Engineers' Handbook*, 7th ed., edited by R. H. Perry (McGraw-Hill, New York, 1997).